UPPSALA
UNIVERSITET

Atomic Scale Design of Clean Energy Materials

Efficient Solar Energy Conversion and Gas Sensing

JAWAD NISAR

ACTA
UNIVERSITATIS
UPSALIENSIS
UPPSALA
2012

Dissertation presented at Uppsala University to be publicly examined in Häggsalen, Ångström Laboratory, Lägerhyddsvägen 1, Uppsala, Friday, September 28, 2012 at 10:15 for the degree of Doctor of Philosophy. The examination will be conducted in English.

Abstract
Nisar, J. 2012. Atomic Scale Design of Clean Energy Materials: Efficient Solar Energy Conversion and Gas Sensing. Acta Universitatis Upsaliensis. *Digital Comprehensive Summaries of Uppsala Dissertations from the Faculty of Science and Technology* 958. 68 pp. Uppsala. ISBN 978-91-554-8436-1.

The focus of this doctoral thesis is the atomic level design of photocatalysts and gas sensing materials. The band gap narrowing in the metal oxides for the visible-light driven photocatalyst as well as the interaction of water and gas molecules on the reactive surfaces of metal oxides and the electronic structure of kaolinite has been studied by the state-of-art calculations. Present thesis is organized into three sections.

The first section discusses the possibility of converting UV active photocatalysts (such as $Sr_2Nb_2O_7$, $NaTaO_3$, $SrTiO_3$, $BiTaO_4$ and $BiNbO_4$) into a visible active photocatalysts by their band gap engineering. Foreign elements doping in wide band gap semiconductors is an important strategy to reduce their band gap. Therefore, we have investigated the importance of mono- and co-anionic/cationic doping on UV active photocatalysts. The semiconductor's band edge position is calculated with respect to the water oxidation/reduction potential for various doping. Moreover, the tuning of valence and conduction band edge position is discussed on the basis of dopant's p/d orbital energy.

In the second section of thesis the energetic, electronic and optical properties of TiO_2, NiO and β-Si_3N_4 have been discussed to describe the adsorption mechanism of gas molecules at the surfaces. The dissociation of water into H^+ or OH^- occurs on the O-vacancy site of the (001)-surface of rutile TiO_2 nanowire, which is due to the charge transfer from Ti atom to water molecule. The dissociation of water into OH^- and imino (NH) groups is also observed on the β-Si_3N_4 (0001)-surface due to the dangling bonds of the lower coordinated N and Si surface atoms. Fixation of the SO_2 molecules on the anatase TiO_2 surfaces with O-deficiency have been investigated by Density Functional Theory (DFT) simulation and Fourier Transform Infrared (FTIR) spectroscopy. DFT calculations have been employed to explore the gas-sensing mechanism of NiO (100)-surface on the basis of energetic and electronic properties.

In the final section the focus is to describe the optical band gap of pristine kaolinite using the hybrid functional method and GW approach. Different possible intrinsic defects in the kaolinite (001) basal surface have been studied and their effect on the electronic structure has been explained. The detailed electronic structure of natural kaolinite has been determined by the combined efforts of first principles calculations and Near Edge X-ray Absorption Fine Structure (NEXAFS).

Keywords: Photocatalysts, Band gap narrowing, Water dissociation, Density functional theory, Gas sensing, Kaolinite

Jawad Nisar, Uppsala University, Department of Physics and Astronomy, Materials Theory, Box 516, SE-751 20 Uppsala, Sweden.

To my beloved parents

List of Papers

This thesis is based on the following papers, which are referred to in the text by their Roman numbers.

I **Hole Mediated Coupling in $Sr_2Nb_2O_7$ for Visible Light Photocatalysis**
Jawad Nisar, Biswarup Pathak, Baochang Wang, Tae Won Kang and Rajeev Ahuja
Phys. Chem. Chem. Phys., 14, 4891-4897 (2012)

II **Band gap engineering by anion doping in the Photocatalyst $BiTaO_4$: First principle calculations**
Jawad Nisar, Baochang Wang, Carlos Moyses Araujo, Antonio Ferreira da Silva, Tae Won Kang and Rajeev Ahuja
International Journal of Hydrogen Energy, 37, 3014 (2012)

III **Band gap engineering in $BiNbO_4$ for visible-light photocatalyst**
Baochang Wang, **Jawad Nisar,** Biswarup Pathak, Tae Won Kang and Rajeev Ahuja
Applied Physics Letters, 100, 182102 (2012)

IV **Study of electronic and optical properties of $BiTaO_4$ for photocatalysis**
Jawad Nisar, Luciana Almeida Silva, Cristiane Gomes Almeida, José Artur Santos Mascarenhas, Baochang Wang, Carlos Moysés Araújo, Rajeev Ahuja, Iuri Pepe, Jailton Souza de Almeida and Antonio Ferreira da Silva
Phys. Status Solidi C, 9, 1593 (2012)

V **Hybrid density functional study on $SrTiO_3$ for visible light photocatalysis**
Peng Liu, **Jawad Nisar**, Biswarup Pathak and Rajeev Ahuja
International Journal of Hydrogen Energy, 37, 11611 (2012)

XIV **Kaolinite: defect states defined material properties – a soft x-ray and first principles study of the band gap**
Annette Pietzsch, **<u>Jawad Nisar</u>**, Erik Jämstorp, Johan Gråsjö, Brian Kennedy, Franz Hennies, Cecilia Århammar, Rajeev Ahuja, and Jan-Erik Rubensson
In manuscript

Reprints were made with the permission from the respective publishers.

Comment on my contributions

The ways I have contributed to the papers in the present thesis are illustrated in the following table. For those papers where I am the first author I have taken the main responsibility in performing calculations, analyzing the data and writing the paper.

Paper	Designing project	Performing calculation	Analysing data	Writting the paper
I	●	●	●	●
II	●	●	●	●
III	●		●	
IV	●	●	●	●
V	●		●	●
VI		●	●	●
VII	●	●	●	●
VIII	●	●	●	●
IX	●	●	●	●
X	●	●	●	●
XI	●	●	●	●
XII	●		●	●
XIII	●	●	●	●
XIV		●	●	●

The following papers are not included in this thesis.

- **Stability of Ferromagnetic Phase in Fe-doped AlH$_3$**
  J. Nisar, R. H. Scheicher, X. Peng and R. Ahuja
  Europhysics Letters, 85, 67006 (2009)

- **Origin of Ferromagnetism in Molybdenum dioxide (MoO$_2$) from ab-initio calculations**
  J. Nisar, X. Peng and R. Ahuja
  Physical Review B 81, 012402 (2010)

- **Theoretical and experimental evidence of enhanced ferromagnetism in Ba and Mn co-substituted BiFeO$_3$**
  O. D. Jayakumar, S. N. Achary, K. G. Girija, K. Tyagi, C. Sudakar, G. Lawes, R. Naik, **J. Nisar**, X. Peng, and R. Ahuja
  Applied Physics Letter 96, 032903 (2010)

- **Stabilizing the defect-induced dilute magnetic semiconductors: Li-doping in GaN with Ga vacancies**
  J. Nisar, X. Peng, T. W. Kang and R. Ahuja
  Europhysics Letters, 93, 57006 (2011)

- **Structure behavior and equation of state (EOS) of Ni$_2$P and (Fe$_{1-x}$Ni$_x$)$_2$P (allabogdanite) from First-principles calculations**
  J. Nisar and R. Ahuja
  Earth and Planetary Science Letters, 295, 578-582 (2010)

- **Equation of state (EOS) and collapse of magnetism in Iron-rich meteorites at high pressure by first-principles calculations**
  J. Nisar and R. Ahuja
  Physics of the Earth and Planetary Interiors, 182, 175-178 (2010)

- **Oxygen- and nitrogen-chemisorbed carbon nanostructures for Z-scheme photocatalysis applications**
  Z. Qian, B. Pathak, **J. Nisar**, R. Ahuja
  Journal of Nanoparticle Research, 14, 895 (2012)

- **Semiconducting Allotrope of Graphene**
  J. Nisar, X. Jiang, B. Pathak, J. Zhao, T. W. Kang and R. Ahuja
  Nanotechnology, Accepted (2012)

- **Excellent ammonia uptake by Li-decorated graphene oxide**
  Y. Li, B. Pathak, **J. Nisar**, Z. Qian and R. Ahuja
  Submitted (2012)

- **Experimental and theoretical evidence of robust room temperature ferromagnetism and half-metallicity in $ZnBi_xO_{1-x}$**
  J. W. Lee, N. G. Subramaniam, **J. Nisar**, J. C. Lee, Y. H. Kwon, J. C. Lee, T. W. Kang, X. Peng and R. Ahuja
  In manuscript

- **Defect-induced room temperature ferromagnetism in B-doped ZnO**
  S. Yılmaz, **J. Nisar**, Y. Atasoy, E. McGlynn, R. Ahuja, M. Parlak, E. Bacaksız
  Submitted (2012)

- **New type of possible high-pressure polymorphism in NiAs-type minerals of the Earth core**
  P. Dera, **J. Nisar**, R. Ahuja, S. Tkachev and V. B. Prakapenka
  Submitted (2012)

Contents

1 Introduction

The search for clean and renewable energy has received great attention due to the depletion of fossil fuel resources and increasing serious environmental problems with their combustion [1, 2]. Hydrogen is one of the most abundant elements on earth and promising energy carrier, which may meet the future world-wide energy demands [3]. Hydrogen has approximately three times the gravimetric energy density as compared to the current fossil fuel [4]. Development of efficient materials for hydrogen production, storage and applications in fuel cells are facing many scientific challenges. Therefore, generation of hydrogen is one of the primary concerns for renewable energy search. Hydrogen is generally combined in water and organic molecules. In order to retrieve the pure hydrogen in elemental form, innovative methods are required for water splitting. On the other hand, solar energy is abundant and one of the very promising energy sources which can be utilized for hydrogen production is photovoltaic cells. Another clean way to produce hydrogen is to dissociate water on the reactive metal oxides/nitrides surfaces of nanostructured materials.

Theoretical atomic scale design of materials for different industrial applications is more economical, cleaner and more efficient than the experimental methods. Computational material science opens up the direction towards the new discoveries and development of novel materials. Many properties and scientific phenomena can be explored or predicted by state-of-art calculations. Atomic scale modeling and modification of the electronic structure by the introduction of foreign elements or creation of defects or converting bulk into nanostructured materials plays an important role for the development of efficient industrial materials.

Photocatalytic process are widely recognized as viable solutions for environmental problems, sustainable clean energy, disinfection of bacteria, self-cleaning and water treatment [5]. In 1972, Honda and Fujishima made the first photovoltaic solar cell of TiO_2 [6] where they could split water into hydrogen and oxygen using ultraviolet (UV) irradiation. Since then, in the last couple of decades, many semiconductor photocatalysis have received attention as a promising solution for energy generation and solve the environmental problems. Recently, metal oxide photocatalyst materials with layered perovskite structures have been studied extensively because of their distinct reaction sites [7-11] for the H_2 and O_2 evolution, respectively. Photocatalytic efficiency requires large enough surface area, a reasonable band

gap, charge separation and lifetime of charge carriers. Mostly, wide band gap photocatalysts such as TiO_2, $Sr_2Ta_2O_7$, $Sr_2Nb_2O_7$, $NaTaO_3$, $KTaO_3$ [9, 12-14] display high photocatalytic activity under UV irradiation because of their high reduction and oxidation powers. One of the key challenges is to design a photocatalyst, which can utilize the maximum portion of sunlight to generate current which are required in the process of water splitting. Sunlight contains only 5 % of the UV and 43 % of visible light. To visualize the enormous potential of harvesting solar energy, it is instructive to follow the sun's electromagnetic energy reaching at the surface of Earth which is plotted by taking the data from American Society for Testing and Materials (ASTM) [15] in *Figure 1*. For maximum utilization of solar visible-light via Photocatalyst Water Splitting (PWS), band gap narrowing is required in a range of wide band gap semiconductors to shift the optical absorption edge from UV to visible region.
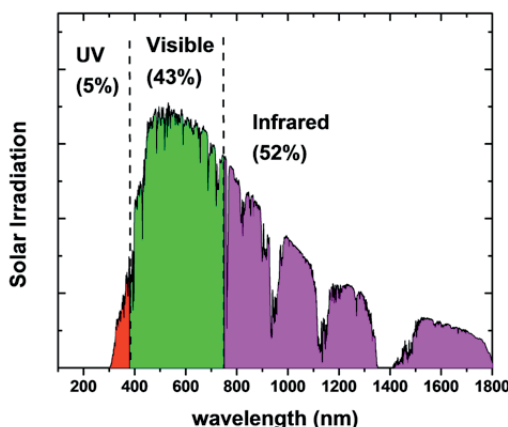
Figure 1. Solar energy spectra [15] illustrating that visible region make up large portion of the solar spectrum.

Many approaches have been used to reduce the band gap and absorb the more abundant visible light of the solar radiation spectrum. Doping of transition metals is one of the approaches to reduce the band gap but in some cases, doped materials suffer from a thermal instability [16], which decreases the life cycle of the photocatalyst. Apart from an appropriate band gap, one of the crucial requirements for water splitting via photocatalyst is that the conduction band minimum (CBM) must be more negative than the reduction potential level and the valence band maximum (VBM) must be more positive than the oxidation potential level. The controlled band gap narrowing can be achieved by the mono or co-doping of suitable anions and cations in the wide band gap semiconductors. Impurity states appear in the band gap and this increases the absorption of solar irradiation, which must be appreciable for a visible-light driven photocatalyst [17]. The position and magni-

tude of the impurity states can be tuned by choosing different combinations and concentrations of dopants [18]. In the first part of this thesis, atomic scale studies of the UV-active photocatalysts have been performed. Visible-light driven photocatalytic activity has been achieved by mono- or co-anionic/cationic doping.

On the other hand, nanostructured metal oxides have been widely used in many industrial applications such as catalysis and chemical sensors [19] due to their large surface to volume ratio. Dissociation of water on the reactive surfaces of metal oxides/nitrides is also very promising for the clean hydrogen production. The reactivity of metal oxides is believed to be governed by oxygen vacancies/vacant anion sites. In this thesis, TiO_2 nanowire and β-Si_3N_4 (0001)-surface have been investigated for the water dissociations due to their high surface reactivity. Chemisorption processes on surfaces are very important for the splitting of water molecules. Apart from water molecules, we have also studied the interactions of many harmful gases such as H_2S, NH_3, SO_2 and NO_2. These molecules are generated in industries and as a result our environmental problems are increasing day by day. The interaction of gas molecules with metal oxide surfaces are also important in other applications such as corrosion, catalysis, photochemistry, electrochemistry and gas sensors [20].

The purpose of this study is to functionalize the oxide surfaces such as TiO_2 (rutile and anatase) by controlling composition and structure through defects. It has been observed that oxygen vacancies on metal oxide surfaces act as preferential adsorption sites for many gas molecules [21, 22]. When oxygen defects appear on the transition metal oxide surfaces, the electronic population of the neighboring cation's d-orbitals is increased due to the neutralization of local charges. Electrons are transferred between the adsorbed gas molecules and the surfaces, which establish the oxidation/reduction reactions on the surfaces. These reduced surface cations provide active sites for the chemisorption of gas molecules. In the second part of my thesis, the effect of defects on the electronic structure, adsorption energy and charge transfer mechanism have been investigated. Water and SO_2 molecules are adsorbed weakly on the defect free surfaces. But chemisorption has been observed due to the charge transfer from the surface to the gas molecules because of different defects. The NiO (100)-surface is one of the promising materials for gas sensing due to its stability and surface reactivity. In this chapter of the thesis, the interaction of NO_2, H_2S and NH_3 molecules with the NiO (100)-surface have been described on the basis of adsorption energy, electronic structure and charge transfer mechanism.

In the final part of my thesis, we have studied the kaolinite ($Al_2Si_2O_5(OH)_4$) material which is a widely spread clay mineral in Earth's crust [23]. It has been commercially used for hundreds of years in applications ranging from ceramics, cosmetics, underground nuclear waste storage, pharmaceutics, and also as a paper coating due to its brightness and adsorp-

tion properties [24, 25]. In order to elucidate its mechanical, thermal, electrical, and optical properties, a proper description of electronic structure is of critical importance. It is very difficult to find pure kaolinite on Earth. Defects have been found to be abundant in natural kaolinite [26] which influence electronic properties. In order to take a closer look to understand the electronic structure of kaolinite, we have used soft x-ray spectroscopy techniques such as Near Edge X-ray Absorption Fine Structure (NEXAFS) and compared with the spectra calculated from state-of-art methods (hybrid functional and GW approach) by involving the effects of the core hole.

2 Computational Methods and Approximations

The main objective of condensed matter physics is to determine the properties of solids such as electronic, optical, magnetic, mechanical, etc. The electronic structure of crystalline materials is not only helpful for the understanding and explanation of experimental findings, but also used for the prediction of properties for the newly designed materials.

This chapter provides information about the computational methods and approximations.

2.1 The Schrödinger Equation

Solid materials are composed of electromagnetically interacting particles with different mass and charge: nuclei and electrons. The non-relativistic Schrödinger equation of the many body system is the foundation of the electronic structure of matter. The Schrödinger Equation is the basic tool for calculating the properties of solids, atoms and molecules. Commonly, the time-independent Schrödinger Equation is used to evaluate the different properties of materials. Time independent equation is given below.

$$H\Psi(\boldsymbol{r}_1, \ldots, \boldsymbol{r}_N, \boldsymbol{R}_1, \boldsymbol{R}_2, \ldots, \boldsymbol{R}_M) = E\Psi(\boldsymbol{r}_1, \ldots, \boldsymbol{r}_N, \boldsymbol{R}_1, \boldsymbol{R}_2, \ldots, \boldsymbol{R}_M) \qquad (2.1)$$

Where H is the Hamiltonian describing all the interactions of the system, E is the total energy of the system and Ψ is the wave function which contains the information of the nuclei and electrons of the atoms in the systems. The Hamiltonian operator can be expressed as follows:

$$H = -\frac{h^2}{2m_e}\sum_i \nabla_i^2 - \sum_I \frac{h^2}{2M_I}\nabla_I^2 + \frac{1}{2}\sum_{i \neq j}\frac{e^2}{|\boldsymbol{r}_i - \boldsymbol{r}_j|} + \frac{1}{2}\sum_{I \neq J}\frac{Z_I Z_J e^2}{|\boldsymbol{R}_I - \boldsymbol{R}_J|}$$

$$-\sum_{i,I}\frac{Z_I e^2}{|\boldsymbol{r}_i - \boldsymbol{R}_I|}, \qquad (2.2)$$

Where M_I, R_I and Z_I are the masses of the nuclei, the corresponding position and nuclear charges, respectively. m_e and $\boldsymbol{r}_i$ are the mass and position of the

electron, respectively. The first term in the equation represents the kinetic energy of the electrons and the second term is the kinetic energy of the nuclei. The following terms correspond to the electron-electron repulsion term and the nuclei-nuclei repulsion term. The last term is the attractive interaction between electrons and nuclei, which is described as an external potential for the electrons.

First, the Born-Oppenheimer approximation has been applied. According to this approximation, since the mass of the electron is much smaller than mass of the nuclei, so the kinetic energy of the nuclei is assumed to be negligible as compared to the kinetic energy of the electron. After employing the Born-Oppenheimer approximation, the Hamiltonian of the electron is written as follows:

$$H = -\frac{h^2}{2m_e}\sum_i \nabla_i^2 + \frac{1}{2}\sum_{i\neq j}\frac{e^2}{|r_i - r_j|} - \sum_{i,I}\frac{Z_I e^2}{|r_i - R_I|}, \qquad (2.3)$$

The electron-electron interactions are not so trivial that it can be solved by the above equation and that's why the density functional theory (DFT), came into the picture which is discussed in the following section.

2.2 Density Functional Theory

In order to solve the many body Schrödinger Equation, a lot of efforts have been made to get the accurate solution of a real system. Hohenberg and Kohn proposed an alternate approach in which an electron charge density plays crucial role for the characterization of the whole system. This approach was later known as Density Functional Theory (DFT). It is based on two fundamental theorems of Hohenberg and Kohn [27, 28]:

Theorem I: It is stated that the ground state density $n(r)$ of the interacting electrons for any system in an external potential $V_{ext}(r)$ determines this potential $V_{ext}(r)$ uniquely. It means that all ground state properties of the system are uniquely determined by the ground state electron density $n_0(r)$.

Theorem II: A universal total energy functional $E[n]$ in terms of the particle density $n(r)$ can be defined as

$$E[\rho(r)] = E_{HF}[\rho(r)] + \int V_{ext}(r)\rho(r)dr \qquad (2.4)$$

$E_{HF}[\rho(r)]$ consists of internal and kinetic energies of all interacting particles in the system. The exact ground state energy of the system is the global min-

imum value of this functional, E_0 and the density, $n(\boldsymbol{r})$ that minimizes the functional, is the exact ground state density, $n_0(\boldsymbol{r})$.

The many body problem is replaced by a single particle problems. The effective potential $V(\boldsymbol{r}_i)$ is elaborated as:

$$V(\boldsymbol{r}) = V_{ext}(\boldsymbol{r}) + \frac{1}{2}\sum_{i \neq j}\frac{e^2}{|\boldsymbol{r}_i - \boldsymbol{r}_j|} + \frac{\delta E_{xc}[n(\boldsymbol{r})]}{\delta n(\boldsymbol{r})} \qquad (2.5)$$

Here, $V_{ext}(\boldsymbol{r})$ is the external potential describing the interaction between valence electrons and the ion cores, the second term is the electron-electron coulomb interaction and the third term is the exchange-correlation term. The exchange correlation functional E_{xc} is not known exactly. To solve this problem, different approximations to the exchange-correlation have been used for the simulation of molecular and solid state physics [29].

2.3 Exchange-correlation Functional

Unknown parameters are assembled in the exchange-correlation term, which must be approximated. The exchange-correlation $E_{xc}(n(\boldsymbol{r}))$ can be split into two parts, the exchange and the correlations, which can be seen as follows:

$$E_{xc}(n(\boldsymbol{r})) = E_x(n(\boldsymbol{r})) + E_c(n(\boldsymbol{r})) \qquad (2.6)$$

The exchange correlation energy functional $E_{xc}(n(\boldsymbol{r}))$ can be approximated by some local functional, dependent on the electron density. Two mainly used approximations for the exchange correlation are described below.

2.3.1 The Local Density Approximation (LDA)

In this approximation, the exchange-correlation functional is derived from the homogenous electron gas [30]. It is the most widely used approximation, defined as:

$$E_{xc}^{LDA} = \int d^3r \, n(\boldsymbol{r}) \, \varepsilon_{xc}^{hom}(n(\boldsymbol{r})) \qquad (2.7)$$

Where $\varepsilon_{xc}^{hom}(n(\boldsymbol{r}))$ is the exchange-correlation energy per particle for a homogenous electron gas with density $n(\boldsymbol{r})$.

LDA approximation has been used very successfully to determine the ground state properties of materials. LDA is must often good for predicting the geometrical quantities such as bond lengths, lattice parameters and mostly gives reliable values of electron densities and vibrational frequencies. But in some systems, LDA overestimates the ground state energies, bond dissociation and adsorption energies as compared to the experimental values. The

band gap of semiconductors and insulators using the LDA approximation always underestimates the experimental values up to 40-50 % or even in some cases, gives no band gap for strongly correlated insulator e.g. NiO [31].

2.3.2 The Generalized Gradient Approximation (GGA)

In the GGA approximation, the exchange-correlation energy contains information from electron density and gradient of density. The generalized gradient approximation based exchange-correlation function is expressed as

$$E_{xc}^{GGA} = \int d^3r \; n(\boldsymbol{r}) \; \varepsilon_{xc}^{GGA}\big(n(\boldsymbol{r}), \nabla n(\boldsymbol{r})\big) \tag{2.8}$$

Since common GGAs are the ones proposed by Perdew, Burke and Ernzerhof (GGA-PBE) [32, 33] and Perdew and Wang (GGA-PW91) [34]. GGA gives better a prediction of bulk modulus, bond lengths, adsorption and binding energies as compared with the LDA, which always overestimates experimental findings. Although the error in the band gap estimation is not resolved with GGA. In this thesis, GGA (PW91 and PBE) has been used for the atomic optimization of materials, since the experimental cell parameters were better reproduced by GGA than by LDA for the investigation of metal oxide systems.

2.4 The Projector Augmented Wave Method

The wave function of the electrons varies considerably in space depending whether the electron is close to the nucleus or far away in the bonding region. In the atomic centered sphere, the wave function oscillates rapidly. Therefore it is suitable to use a partial wave expansion to describe this region. The wave functions have smooth variation outside the augmented region, thus the electrons are described by plane waves or some other convenient basis set. The partial solutions of the different regions are matched at the boundary between the atomic and the interstitial regions.

The Projector Augmented-wave method (PAW) method is based upon a linear transformation operator, T which transfers the all electron wave function, $\boldsymbol{\Psi_n}$ to a pseudo wave function, $\widetilde{\boldsymbol{\Psi}}_{\mathbf{n}}$

$$|\boldsymbol{\Psi_n}\rangle = T|\widetilde{\boldsymbol{\Psi}}_{\mathbf{n}}\rangle \tag{2.9}$$

For each augmentation regions, both $|\boldsymbol{\Psi_n}\rangle$ and $|\widetilde{\boldsymbol{\Psi}}_{\mathbf{n}}\rangle$ can be represented as linear combination of partial waves.

$$|\mathbf{\Psi_n}\rangle = \sum_i c_i |\phi_i\rangle \tag{2.10}$$

$$|\widetilde{\mathbf{\Psi}}_\mathbf{n}\rangle = \sum_i c_i |\tilde{\phi}_i\rangle \tag{2.11}$$

The transformation operator, T is defined as

$$T = \left[1 + \sum_i (|\phi_n\rangle - |\tilde{\phi}_n\rangle) \right] \langle \tilde{p}_i| \tag{2.12}$$

Where $\langle \tilde{p}_i|$ is the projection function which can be generated from different practical schemes. The pseudopotentials are directly related to the all-electron wavefunction. There are various types of pseudopotentials, in which the main purpose is the replacement of a rapidly oscillating wave function with a smooth pseudopotential [35]. The PAW has combined features of the ultra-soft pseudopotentials [36] and the linear augmented-plane-wave [37] methods . In this thesis, the PAW [38] has been used which is implemented in the Vienna *ab-initio* simulation package (VASP) [39].

2.5 Band Gap Problems

It is well known that standard DFT exchange-correlation (XC) functionals (LDA/GGA) dramatically underestimates the band gaps, for semiconductors and insulators, which is related to the so-called "derivative discontinuity" in the exchange correlation potential [32]. The band gap is not a well-defined ground state property. The Kohn-Sham (KS) formalism fails to predict the excitation energies of semiconductors and insulators [40]. To correct the band gap, one approach is the scissors operator, in which the conduction band is shifted upward to match the band gap with experimental values. It is however not a good method to predict the electronic structure of unknown materials. The GW method describes the excited states and predicts a better band gap but it is not possible for big supercells because of its computational cost. Another method is LDA+U, where orbital dependence of the coulomb and exchange interaction has been considered, which are not available in LDA/GGA. This method also improves the ground state properties. Hybrid functional approximation also plays an important role for the prediction of the accurate electronic structure of materials. In this approach, the screened HF potential is combined with the both short and long range screened density functional. The above approaches have been suggested to decrease the error in the band gap of semiconductor and insulators.

2.5.1 Correlation and Hubbard U

LDA and GGA fail to explain the strong correlated materials, such as those containing elements with partially filled valence *d* or *f*-states. The Mott-Hubbard insulators and *4f* rare earth compounds are predicted as metals using LDA and GGA approximations (e.g. NiO) but actually these are insulators. The correlation part of the DFT exchange correlation function (LDA, GGA, etc) is not described accurately enough for the localized states such as *3d* and *4f*. Improvement in the correlation function is required to better prediction of electronic and optical properties. The parameter U is used as an on-site replacement of LDA or GGA to improve the description of localized 3d or 4f states. This approach is called as LDA+U method. The Coulomb *U* is the energy difference between removing an electron from the occupied state to vacuum and that of adding an electron to the unoccupied states from vacuum, referenced to the energy of the unperturbed system. If a correct Coloumb *U* is chosen then the LDA+U approach will not only improve the description of the electronic structure but may also improve ground state properties such as lattice parameters and magnetic moments. The generalized LDA+U total energy functional take the form as follows [41, 42]:

$$E^{LDA+U}[\rho^\sigma(\boldsymbol{r}), n^\sigma] = E^{LDA}[\rho^\sigma(\boldsymbol{r})] + E^{ee}[n^\sigma] - E_{dc}[n^\sigma] \qquad (2.13)$$

Where $E^{LDA}[\rho^\sigma(\boldsymbol{r})]$ is the usual local spin-density functional of the total electron spin densities, $\rho^\sigma(\boldsymbol{r})$. $E^{ee}[n^\sigma]$ is an electron-electron interaction energy and $E_{dc}[\rho^\sigma]$ is a ''double counting'' term, which accounts approximately for an electron-electron interaction energy already included in E^{LDA}.

$$E_{dc}[\rho^\sigma] = \frac{U}{2} n(n-1) - \frac{J}{2} \sum_\sigma n^\sigma (n^\sigma - 1) \qquad (2.14)$$

Where, U and J are the screened coulomb Hubbard and exchange parameters, respectively. LDA+U method is implemented in VASP. In paper XII, the GGA+U method has been applied to characterize the electronic structure of NiO (100) surface with the adsorption of different gas molecules.

2.5.2 Hybrid Density Functionals

It is well known that either GGA and LDA nor Hartee Fock (HF) reliable for predicting the accurate band gaps of semiconductors and insulators, while hybrid functionals generally provides a better estimation of the band gap. GGA/LDA also fails to describe localized electrons in both solids materials and molecules. The electronic correlation is represented by the corresponding part of PBE density functional. Thus, the resulting exchange correlation energy expression for PBE0 takes the following form.

$$E_{xc}^{PBE0} = aE_x^{HF} + (1-a)E_x^{PBE} + E_c^{PBE} \qquad (2.15)$$

For the PBE0 hybrid function, this mixing parameter is set to $a = 1/4$, which is determined by perturbation theory [43, 44].

To improve the local and semi local density approximations, a well-established strategy of hybrid functional is implemented [44, 45] that includes a certain amount of nonlocal Hartree-Fock exchange. Coulomb operator can be split into short-range (SR) and long range (LR) parts, which are separated by a decomposition of the electron-electron interaction, and can be seen as:

$$\frac{1}{r} = \frac{erfc(\mu r)}{r} + \frac{\text{erf}(\mu r)}{r} \qquad (2.16)$$

Here $erfc(\mu r) = 1 - \text{erf}(\mu r)$ and μ is an adjustable parameter governing the extent of short range interactions. If $\mu = 0$, the long-range term becomes zero and the short range term is equivalent to the full Coulomb operator. The opposite is true for $\mu = \infty$. The PBE0 exchange functional split into short range and long range parts is given below:

$$E_x^{PBE0} = aE_x^{HF,SR,\mu} + aE_x^{HF,LR,\mu} + (1-a)E_x^{PBE,SR,\mu} + E_x^{PBE,LR,\mu} \\ - aE_x^{PBE,LR,\mu} \qquad (2.17)$$

SR and LR denote the short and long range parts of the respective exchange interactions (PBE and HF exchange). μ values indicate that the HF and PBE long range exchange contributions to this functional are rather small, and these terms tend to cancel each other. Therefore, after neglecting these two terms, the Heyd-Scuseria-Ernzerhof (HSE) based on screened Coulomb hybrid density functional has been obtained, which is described as follows:

$$E_{xc}^{HSE} = aE_x^{HF,SR,\mu} + (1-a)E_x^{PBE,SR,\mu} + E_x^{PBE,LR,\mu} + E_c^{PBE} \quad (2.18)$$

μ is the range-separation and lies between 0.2 and 0.3 Å^{-1} for the HSE method, If the screening parameter μ is set to 0.2 Å^{-1}, this confirms to the HSE06 scheme. In this thesis, the HSE06 method has predicted better band gap estimation for some oxides such as $Sr_2Nb_2O_7$, $NaTaO_3$ as compared to the PBE0. But in other cases like $SrTiO_3$, PBE0 gives good agreement with experimental results. Both methods are implemented in the latest version of VASP.

2.5.3 GW Approximation

Many body perturbation theories are used to determine quasiparticle excitations in solid materials, especially for accurate calculation of electronic band structure. In the GW approximation, HF- approximation has been replaced the exchange correlation which is based on the concept of screened Coloumb interaction [46]. By the introduction of the screening of interaction between particles in a many body system, this leads to the concept of quasiparticles. A quasiparticle is defined as it is simply an electron with the screening cloud [47]. The qauasiparticle energies and wave functions are obtained by solving [48]:

$$(T + V_{ext} + V_H)\emptyset_{nk}(\boldsymbol{r}) + \int d^3r'\,\Sigma\,(\boldsymbol{r}, \boldsymbol{r}', E_{nk})\emptyset_{nk}(\boldsymbol{r}')$$
$$= E_{nk}\emptyset_{nk}(\boldsymbol{r}) \tag{2.19}$$

In the GW approximation, the self-energy operator, Σ is described as a product of the Green's (G) function and the screened Coulomb kernel, W.

$$\Sigma(\boldsymbol{r}_1, \boldsymbol{r}_2, \omega) = i \int d\omega'\,G(\boldsymbol{r}_1, \boldsymbol{r}_2, \omega - \omega')W(\boldsymbol{r}_1, \boldsymbol{r}_2, \omega') \tag{2.20}$$

Where $G(\boldsymbol{r}_1, \boldsymbol{r}_2, \omega)$ is the two-particle Green,s function, which describes the particles at $\boldsymbol{r}_1$ and $\boldsymbol{r}_2$, and W is the the screened Coulomb interaction. Here, The Green's function is then given in terms of the quasiparticle wave functions:

$$G(\boldsymbol{r}_1, \boldsymbol{r}_2, \omega) = \sum_i \frac{\emptyset_i^{KS}(\boldsymbol{r}_i)\emptyset_i^{KS*}(\boldsymbol{r}_2)}{\omega - E_i^{KS} \pm i\delta} \tag{2.21}$$

V_C, is the Coulomb interaction, which is screened by the full time-ordered dielectric constant, ϵ^{-1} and the screened Coulomb interaction is given below:

$$W(\boldsymbol{r}_1, \boldsymbol{r}_2, \omega') = \frac{1}{\Omega} \int d^3r'\,\epsilon^{-1}(\boldsymbol{r}_1, \boldsymbol{r}', \omega')V_C(\boldsymbol{r}' - \boldsymbol{r}_2) \tag{2.22}$$

In this approximation, $G(\boldsymbol{r}_1, \boldsymbol{r}_2, \omega)$ is constructed by using the wave functions and band energies of the LDA/GGA. For the calculation of the screened Coulomb interaction, a full dielectric matrix is required. The dielectric matrix is obtained from density-functional theory. The GW-approximation has been implemented in the latest version of VASP.

2.6 Other Computational Tools

2.6.1 Work Function Calculations

The work function is defined as "The minimum energy needed to remove an electron from the Fermi level to infinity". The work function can be calculated using the density functional methods and it is defined as [49, 50].

$$Work\ function = \ \phi = V(\infty) - E_F \qquad (2.23)$$

Where, $V(\infty)$ and E_F are the electronic potential in a vacuum region far from the neutral surface and the Fermi energy of the neutral surface system, respectively. We have calculated work function for many systems and one such example is $BiNbO_4$ where we have constructed the $BiNbO_4$ (100)-surface with a vacuum space of 12 Å for the calculations of vacuum potential, $V(\infty)$. It was calculated from the plot of planar-average electrostatic potential energy along the direction of stable surface which are shown in *Figure 2* (i.e. the value in the middle of the vacuum from the plot).
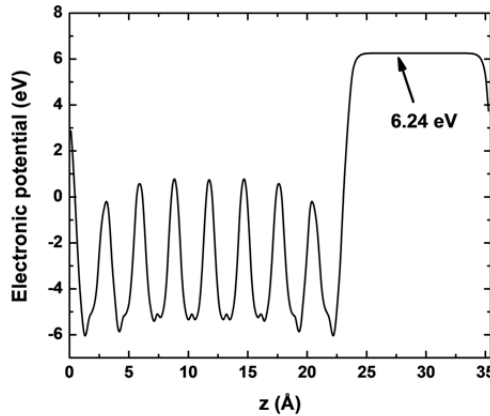

Figure 2. Calculated electrostatic potential profile of $BiNbO_4$ slab system in which the planar-averaged electrostatic potential is plotted as a function of cell dimension normal to the surface.

In paper II, III & IV, the work functions of $BiTaO_4$ and $BiNbO_4$ have been calculated which is the common reference for the band edge alignment. The band levels of the semiconductors and the redox potential levels are plotted with respect to the common reference point. The reduction reaction potential (-4.44 eV) and oxidation reaction potential (-5.67 eV) [51] are aligned with respect to the band edges which is very crucial for the water splitting via a photocatalyst.

2.6.2 Z+1 Approximation

Z+1 approximation [52] is used to describe the core hole effect in the solids for the comparison of the electronic structure with the experimental XAS and Near Edge X-ray Absorption Fine Structure (NEXAFS) data. The Z+1 approximation has been successfully applied to evaluate the core hole effect in both the finite molecules and solids [53, 54]. In this thesis, the core hole is achieved by replacing the regarded atom e.g. oxygen by the next heaviest element in the periodic table e.g. fluorine and removing one electron from this element, the main limitation of this approximation is the treatment of the core electrons within the Projected Augmented Wave (PAW) method [38] in which the frozen core approximation is applied. Recently, this method has been successfully applied on amorphous Al_2O_3 to describe the electronic structure and coherence between calculated and experimental measured NEXAFS [55] was found. In paper XIV, this method was applied for the description of defect states in the forbidden gap of kaolinite and compared with experimental findings.

2.6.3 Optical Properties

The absorption of photons in solid materials involves two kinds of electronic excitations, namely interband and intra-band transitions. Interband transition, in which electrons are excited from the valence band to conduction band and creating holes in the valence band. While, Intraband transition is the transition between the quantized levels within the valence or conduction band. The perturbation theory has been applied for the complex dielectric function calculations, where the unperturbed part of the Hamiltonian is the crystal Hamiltonian and the light field is treated as the perturbation. The electric dipole approximation is used and the imaginary part of the dielectric function becomes [56]

$$\varepsilon_2^{ij}(\omega) = \frac{4\pi^2 e^2}{\Omega m^2 \omega^2} \sum_{\boldsymbol{knn'}} <\boldsymbol{kn'}|p^i|\boldsymbol{kn}><\boldsymbol{kn'}|p^j|\boldsymbol{kn}> \delta(E_{\boldsymbol{kn'}} - E_{\boldsymbol{kn}} - \hbar\omega)$$

(2.24)

Where, p is the momentum operator, e is the electron charge, m its mass, Ω is the volume of the crystal and δ is the crystal wave function corresponding to the nth eigenvalue E_{kn} with crystal wave vector $\boldsymbol{k}$. The absorption curves can be obtained from the imaginary part of the dielectric constant using Kramers-Kroning dispersion relations [57]. It is well known that DFT does not provide any good results for this kind of excitation spectra because it cannot calculate the excited states properly. In this thesis, the absorption curves can be obtained from the imaginary part of the dielectric constant using GGA-PBE and hybrid functional.

2.6.4 Defect Formation Energy

To study the formation of intrinsic or extrinsic defects, the formalism of the defect formation energy has been employed, which is defined as [58, 59]:

$$\Delta E_f(D^q, E_F, \mu) = E_T(D^q) - E_T(H) + \sum_i n_i \left(\mu_i^{elem} + \Delta\mu_i\right) + q(\Delta E_F + E_V) \quad (2.25)$$

Here, $E_T(D^q)$ and $E_T(H)$ are the total energies of defect containing and pristine system, respectively. In the third term, n_i is the number of atoms removed or added to create the defects in the system and $\left(\mu_i^{elem} + \Delta\mu_i\right)$ is the chemical potential of the particle reservoir, in which μ_i^{elem} is the total energy of the atom i, in the Stable-Element Reference (SER) state at 0 K. The final term takes the dependence of the defect formation energy on the charge state, q and energy of the valence band, E_V into account. For neutral native point defects, the charge $q = 0$ and the last term in the above equation is omitted. In paper IX, Intrinsic defects such as Ti-vacancy and O-vacancy have been considered on the surfaces of TiO_2 nanowire. The following relation needs to be satisfied for the allowed thermodynamic process,

$$\Delta H_{TiO2} = \Delta\mu_{Ti} + 2\Delta\mu_O \quad (2.26)$$

If the O-vacancy in TiO_2 is considered, the defect formation energy for the neutral defect can be calculated as follows:

$$\Delta F_f\left(TiO_{2(1-x)}\right) = E_T\left(TiO_{2(1-x)}\right) - E_T(TiO_2) + x\left[\mu_O^{elem} + \Delta\mu_O\right] \quad (2.27)$$

Extreme equilibrium growth conditions such as O-rich and O-poor have been applied. The O-rich environment is the most probable to occur in a natural environment or ambient conditions. In case of O-rich conditions, $\Delta\mu_O = 0$ and then $\Delta\mu_{Ti} = \Delta H_f(TiO_2)$ and in the other extreme O-poor environment, $\Delta\mu_O = \frac{1}{2}\Delta H_f(TiO_2)$ and $\Delta\mu_{Ti} = 0$. The above defect formation energy formulation has been used in paper IX and XI to simulate the defects on TiO_2 surfaces at different growth conditions.

2.6.5 Compensation of Charged Defects

Sometimes, neutral defect states would no longer correspond to the lowest energy states and would not give us the right physics of the defect formation. Thus, the last term in equation (2.25), is very important to include for the charge defect simulation. To get a better picture of the intrinsic defect formation, defects charge compensation approach has been applied. In paper XIII, oppositely charged defects compensate each other and pin the Fermi energy at the energy of the formation for compensating defects in kaolinite,

which is different to that of the neutral defects. Therefore, the total energy of the positively charged V_{OH} and the negatively charged V_H and O_H defects within PBE and HSE06 methods were calculated. The defect formation energy, calculated by PBE and HSE06, as a function of Fermi energy for the V_H, V_{OH}, and O_H defects in different charge states are shown in *Figure 3*.
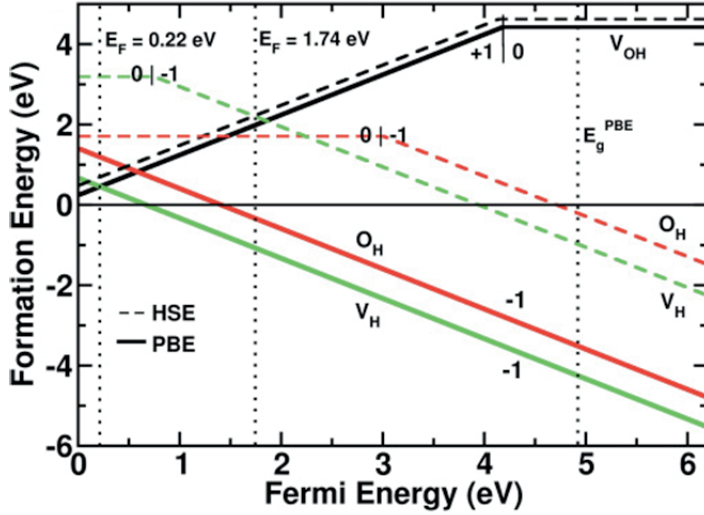

Figure 3. The PBE (full line) andHSE06 (dashed line) defect formation energy as a function of Fermi energy for the three different defects V_{OH}, O_H and V_H. The vertical dotted line denotes the lowest energy intersections of the acceptor and donor defects with PBE and HSE06, respectively. Reprinted from the paper XIII with the permission of the publisher.

3 Band Gap Engineering for Visible-light Photocatalyst

3.1 Photocatalytic Water Splitting Process

The foremost concern of the photocatalytic semiconducting materials is to use the major part of the solar spectrum (especially the visible part) to split the water into hydrogen and oxygen. Thus, the photon energy of the incident solar lights should be higher than the band gap of the semiconductor so that the electrons can be excited from the valence band to the conduction band and generate holes in the valance band. Therefore as the semiconductor is irradiated by light, negatively charged electrons (e^-) and positively charged holes (h^+) are created in the bulk semiconductor and this state is called the photo-excited state. These excited electrons and holes should be separated and moved towards the surface reaction sites otherwise they will recombine and dissipate the energy in the form of heat. The water splitting process becomes more favorable when the electron-hole recombination is reduced so that the water molecules get the chance to react with the electrons and holes to generate hydrogen and oxygen respectively. Usually the solvated protons are reduced to form hydrogen. A schematic diagram of the water splitting process using a photocatalyst is presented in *Figure 4*.
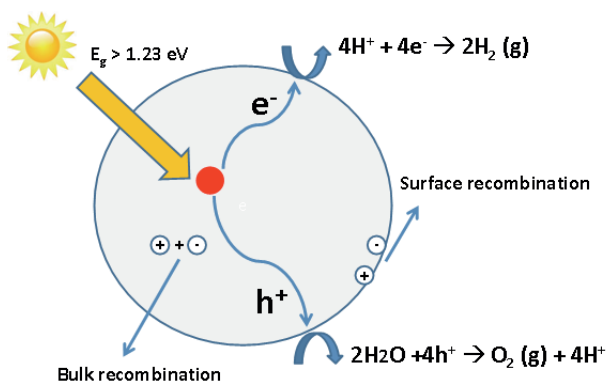

$E_g > 1.23$ eV

$4H^+ + 4e^- \rightarrow 2H_2$ (g)

e^-

Surface recombination

h^+

$2H_2O + 4h^+ \rightarrow O_2$ (g) $+ 4H^+$

Bulk recombination

Figure 4. Main process of photocatalytic water splitting into hydrogen and oxygen.

In the photo catalysis, the minimum cell potential required to split the water into hydrogen and oxygen is 1.23 eV which can be related to the Gibbs free energy change using the following equation ($\Delta G^0 = -nFE^0$) [60].

$$H_2O \rightarrow \frac{1}{2}O_2 + H_2 \; ; \qquad \Delta G = 1.23 \; eV \qquad (3.1)$$
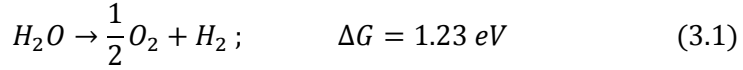
Therefore, the band gap of the photocatalytic materials should be larger than 1.23 eV to facilitate the spontaneous water oxidation and reduction reactions. Absolute value of the reduction (H^+/H_2) and oxidation (H_2O/O_2) potential levels for H_2O should be located inside the band gap for water splitting into H_2 and O_2. The lowered band gap (harvest maximum solar light) does not guarantee to improve the H_2 evolution efficiency because water splitting also depends upon the reduction and the oxidations powers. The reaction rate for the generation of hydrogen and oxygen via solar-light irradiation depends upon the reduction (Δ_1) and the oxidation powers (Δ_2) of the photocatalysts, as presented in *Figure 5*. Here, E_1 and E_2 denote the reduction and oxidation potential levels, respectively. The reducing power (Δ_1) is defined as the energy difference between the conduction band minimum (CBM) and reduction potential level (E_1), and the oxidizing power (Δ_2) is the energy difference between the valence band maximum (VBM) and oxidation level (E_2) [61]. Thus, the reaction rate of the photocatalysis process depends upon the concentration of reactants and reaction rate constant. In case of water splitting reactions, it could be assumed that the concentrations of reactants are constant because the incident light is the same and the production of the electrons and holes are constantly available for the redox reactions.
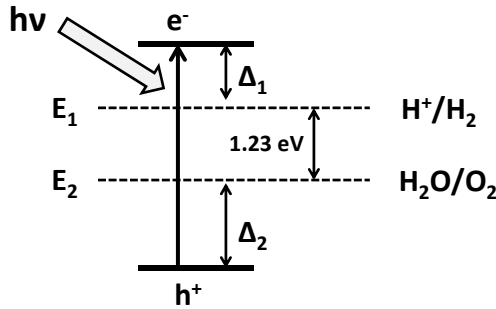

Figure 5. Schematic diagram for the reducing and oxidizing power for photocatalyst.

The rate constant (λ) of any chemical reaction can be calculated from the Arrhenius equation [61]:

$$\lambda = Ae^{-E_a/RT} \qquad (3.2)$$

Where, E_a is the activation energy at the temperature T, A is the pre factor and R is the gas constant. Maximum efficiency can be achieved for the water

splitting if the reaction rate of the reduction and the oxidation reactions are same. All parameters in the above equation are constant expect the activation energy (E_a). In the photocatalytic reaction, reducing and oxidizing powers are represented by the activation energy. So, the condition for the maximum efficiency of the photocatalytic process is $\Delta_1 = \Delta_2$. Other than the thermodynamic factors, the efficiency of photocatalyst can be changed by changing the pH of the solutions [62], as the reduction and oxidation potential levels can be tuned by the variation of pH of the solution. The stability of the photocatalytic materials is also changed with pH of the solution. In this thesis, this parameter is not considered for the designing of efficient photocatalyst.

3.2 Requirements for an Efficient Photocatalyst

For the development of efficient visible-light driven photocatalysis, some important conditions are summarized as following.

- The photocatalyst materials should have a sufficient band gap (1.7 eV < E_g < 2.1 eV) to harvest the visible light.
- The position of the band edges should be aligned with respect to the reduction and oxidation potential levels. The conduction band minimum (CBM) has to be more negative than the reduction potential (H^+/H_2), while the valence band maximum (VBM) has to be more positive than the oxidation potential (H_2O/O_2).
- Photogenerated electrons and holes separation and migration towards the surfaces should be fast in order to avoid bulk/surface recombination [20].
- The stability of the photocatalytic materials should be high in the photo-induced environment. Photocorrosion is considered to be the main reason causing the poor stability of photocatalysts. As some materials such as ZnO or CdS get oxidized in the presence of the holes they thus become unstable in the solution. [63]. The photocorrosion reactions for CdS and ZnO occur as follows:

$$CdS + 2h^+ \rightarrow Cd^{2+} + S \qquad (3.2)$$

$$ZnO + 2h^+ \rightarrow Zn^{2+} + \frac{1}{2}O_2 \qquad (3.3)$$
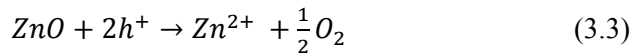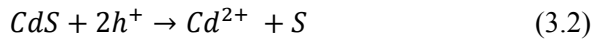
Sometimes the photo generated hydrogen and oxygen on the photocatalyst surfaces reacts back to form water, which is called "surface back reaction (SBR)", which decreases the efficiency of the photocatalyst. To avoid the SBR, electron donor and acceptor sacrificial reagents have been involved in the photocatalyst environment. The separation of reaction sites on the sur-

face of photocatalyst materials can also depress the formation of H_2O from H_2 and O_2. The layered perovskite structures such as $Sr_2Nb_2O_7$, $Sr_2Ta_2O_7$ are good candidates for the separation of reduction and oxidation reaction sites, which might be increased the efficient of water splitting.

3.3 UV-active Photocatalyst Materials

The investigation of water splitting mechanism is important for efficient hydrogen production. The most important aspects of the photocatalyst are the reasonable band gap and the band positions with respect to the water oxidation/reduction potentials. Recent studies show that photocatalyst materials consisting of d^0 metal cations (Nb^{5+}, Ta^{5+}, Ti^{4+}) have reasonable activities for water splitting. Experimentally, many wide semiconductor metal oxides materials such as $Sr_2Nb_2O_7$ [9, 64], $NaTaO_3$ [65], $SrTiO_3$, $BiNbO_4$ [66, 67] and $BiTaO_4$ [67, 68] exhibit efficient photocatalytic activities for hydrogen and oxygen production from water under UV irradiation. Valence band of these photocatalyst materials consists of mainly O *2p* orbitals, which is more positive than oxidation level and conduction band edge contains mainly d-orbitals of Ta, Nb or Ti is more negative than reduction (shown in *Figure 6*). The main difference in the photocatalytic properties between tantalates and niobates is mainly due to the conduction band levels (Ta *5d* and Nb *4d*) because Ta *5d* is more negative than Nb *4d*. Unfortunately, the development of UV driven photocatalyst are limited when it comes to large scale hydrogen production in the presence of sun light since the solar spectrum contains only 5 % of UV light. Whereas Visible-light part of the solar light is more dominated (43 %). Thus, it is more important to design an efficient photocatalyst in the visible region. Therefore, the development of visible-light driven photocatalyst becomes a very promising topic for the efficient water splitting.

In this work, it is observed that the electronic structure and absorption spectra are affected by the various foreign dopants in the UV active photocatalysts. The absolute bands positions of the various UV active photcatalyst have been controlled by different approaches of band gap engineering. In *Figure 6*, it is observed that these materials have stronger reducing and oxidizing power as compare to the TiO_2 [69], except $SrTiO_3$ who has almost same reducing power as TiO_2.
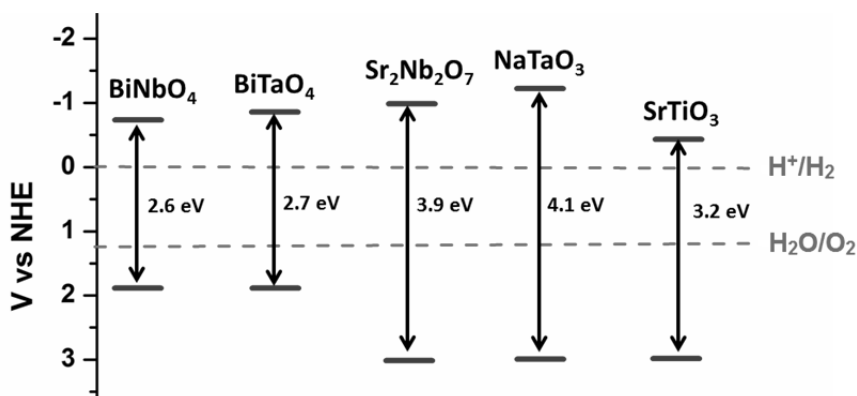
Figure 6. Schematic diagram in which the valence and conduction band edge positions are aligned with respect to redox potential levels for water splitting [9, 70, 71].

3.4 Tuning of Band Gap

The solar-conversation efficiency is low when the solar spectrum and the optical absorption spectra of the photocatalytic semiconductors are mismatched. This becomes significantly low for the wide band gap semiconductors. So the band gap tuning is very important in the wide band gap semiconductors used for efficient visible-light photocatalyst. In the following list, a couple of methods are very effectively used for the band gap engineering.

- Quantum size effect [61]
- Introduction of intrinsic defects
- Foreign elements doping

In this part of the thesis, the focus is on the modification of electronic structure and optical properties by the doping of foreign elements to increase the solar-energy conversion efficiency.

3.5 Modification in Band Gap by Doping

In order to develop the water splitting under visible-light irradiation, suitable modification in band gap is required. Band gap engineering of wide band gap semiconductors have been extensively used to achieve visible-light absorption and subsequent photocatalytic activity [72-74]. Generally, the conduction band of metal oxide semiconductors is composed of *d*-states of cations and valence band consisting of the O *2p* orbitals. Thus, there are two ways to reduce the band gap of semiconductors. Either by shifting the valence band upward or moving the conduction band downwards. Therefore,

the tuning of valance band can be done by anionic doping. Similarly, the conduction band position can be tuned by cationic doping. Such foreign doping elements create donor or acceptor states in the band gap. The donor levels are created above the valence band and the acceptor levels just below the conduction bands. Strategies of the band gap narrowing by the induction of impurity levels in the band gap, shown in the *Figure 7*.
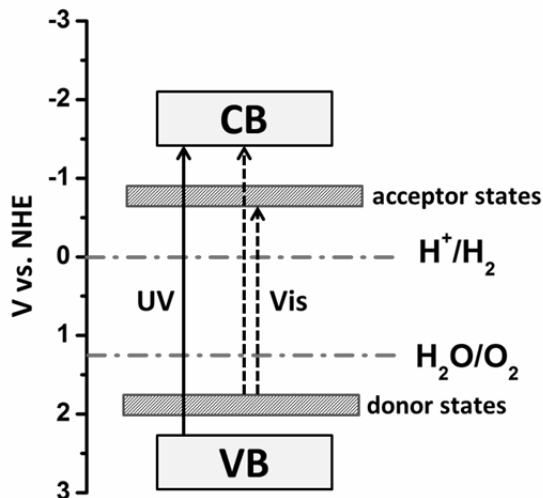

Figure 7. Strategies of band gap narrowing by doping for the designing of efficient visible-light driven photocatalyst.

3.5.1   Anionic Mono-doping

The valence band of metal oxide photocatalysts mainly consist of O *2p* states. Nonmetals such as nitrogen, carbon, phosphorous and sulfur have larger p-orbital energy as compared to the oxygen p-orbital energy [75]. Thus, the doping of C, N, P, or S in place of O, shifts the valence band edge upwards and narrow the band gap, which can be suitable for visible-light driven photocatalyst.

For further analysis of the dopant effects on the electronic structure, the anionic doping in the layered perovskite $Sr_2Nb_2O_7$ has been considered (paper I). The calculated band gap of the pristine $Sr_2Nb_2O_7$ is 2.46 eV using GGA-PBE method. But the GGA underestimates the band gap [76]. To overcome this problem, the hybrid functional method HSE06 has been used. Using the HSE06 method, the calculated band gap of the pure system is 3.92 eV, which is in excellent agreement with the experimental value of 3.9 eV [9]. This wide band gap semiconductor is reported to be absorbing less than 3 % of visible-light so the band gap engineering in this system is very important to improve the maximum utilization of solar irradiation. Therefore, the choices of the dopant elements are very important for the designing of

efficient photocatalysts. In case of $Sr_2Nb_2O_7$, the potential of valence band is deep enough to oxidize water into O_2, so modification or shifting of the valence band is more critical than the conduction band. Thus, considering doping of sulfur, nitrogen, phosphorus and carbon are the strong candidates for the band gap narrowing. The total density of states of doped systems is illustrated in the band gap narrowing mechanism by anionic doping (*Figure 8*). The effect of anionic mono-doping on the electronic structure and optical spectra of the wide band gap semiconductors have been evaluated for the maximum absorption of the solar light.
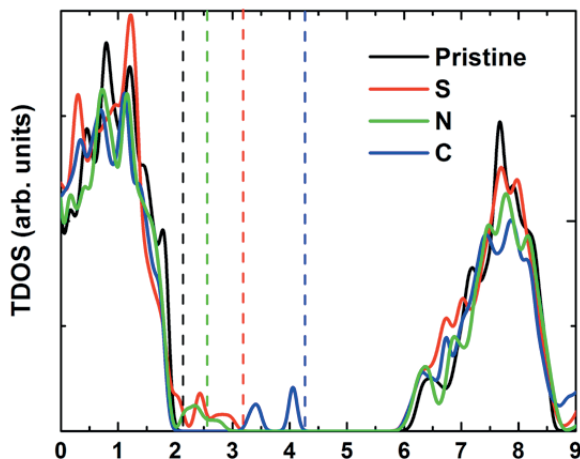
Figure 8. Total density of states (TDOS) for anionic-doped $Sr_2Nb_2O_7$ (using HSE06 method) and compared with the pristine structure. The vertical lines indicate the Fermi level.

It indicates that impurity states appear in the band gap which narrows the effective band gap. In case of nitrogen/phosphorous doping in the substitution of oxygen, holes are generated in the system. Partially occupied states appear at the valence band edge, which contains a mix of O *2p* and N *2p*/P *3p* orbitals. These partial occupied states at the Fermi level trap the photogenerated electrons, which might facilitate the recombination losses. Sulfur has the same number of valence electrons as oxygen, but the S *3p* orbital energy is larger than O *2p,* which shifts the VBM upwards. Carbon has two less valence electrons than the host oxygen atoms, so two holes are induced in the system. These states act as double acceptor levels. The distance between the doped C atom and the nearest-neighboring O atom is 1.48 Å. It indicates that a strong coupling exists between C and the nearest O, which leads to the distorted geometry that is not favorable as compared to the other anionic dopants. The formation energies of anionic mono-doping are calculated and it is found that sulfur is the most favorable dopant as compared to the other anionic dopants. The reason might be that sulfur is isoelectronic to

oxygen atom whereas N and C introduce single and double holes in the system, respectively and thus destabilize the system. The drawback of mono-doping is either limited by band gap narrowing or by creating unoccupied impurity states in the band gap. Therefore, such mono-doping might be good for the optical absorption of visible solar light but it increases the concentration of recombination centers.

3.5.2 (Anion-Anion) Co-doping

Mono anionic doping in semiconductors generates defect levels above the VBM, which behave as recombination sites. Such impurity states can be removed if the double holes mediated coupling can be introduced. Therefore, Co-doping of anionic dopants such as N, P, C or S have been considered, which can add more holes to the system so that the strong coupling is achieved through lattice relaxation [77, 78]. In case of anion-anion co-doping, fully filled bands appear above the VBM, leading to narrow the band gap, which is more effective as compare to the mono-doping.
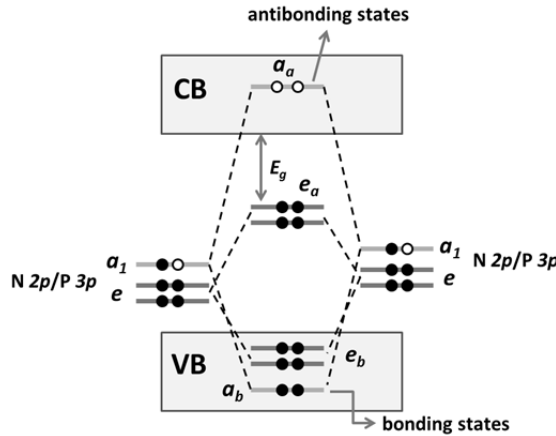
Figure 9. Schematic diagram for the description of double holes mediated coupling by the substitution of anions such as N, P, C and S at O-sites.

Schematic diagram of double holes mediated coupling mechanism for the substitution of anions at the O sites are presented in *Figure 9*. In metal oxides materials, mono-doping of N, C, S or P creates impurity states above the VBM because of their higher *2p* (N, C) or *3p* (S, P) orbital's energy comparing to the O *2p* orbital's energy. These impurity states are occupied or partial occupied or unoccupied depending on the dopants. Due to the low symmetry at the O sites, the impurity p-orbital energy levels split into a_1 and e states, as shown on the left and the right panels in *Figure 9* [77, 78]. When dopants are placed very close to each other with two net holes, a_1 of p-orbitals of anionic dopants form bonding (a_b) and antibonding states (a_a) lying deep in the va-

lence band (VB) and the conduction band (CB), respectively. Interaction of two fully occupied states (e) will induce an upward shift in the occupied e_a state and a downward shift in the filled e_b states. Therefore, the new effective band gap (E_g) is measured from the e_a state to the CBM. It is expected that (anionic-anionic) co-doping leads to a larger reduction in band gap as compare to the mono-doping, owing to the double holes mediated coupling.

In paper I-III and V, double holes mediated coupling mechanism on the $Sr_2Nb_2O_7$, $BiTaO_4$, $BiNbO_4$ and $SrTiO_3$ has been applied for significant band gap reduction. The band gap of some semiconductors with mono-doping or co-doping of anions (S, N, P or C) is presented in the Table 1. In case of double holes anionic coupling, clean band gap is achieved, which can reduce the recombination losses.

Table 1. *Band gaps of pristine, anion mono-doped, and co-doped $Sr_2Nb_2O_7$, $SrTiO_3$, $BiTaO_4$ and $BiNbO_4$ using GGA-PBE method, the band gaps are also calculated by the state-of-art hybrid functional method (HSE06 or PBE0) are presented in the parenthesis.*

Dopants	$Sr_2Nb_2O_7$	$SrTiO_3$	$BiTaO_4$	$BiNbO_4$
Pristine	2.46 (3.92)	1.81 (3.25)	2.4	2.54
S	1.45 (2.61)	1.29 (2.72)	2.28	2.1
N	1.89	1.38 (2.12)	2.13	2.29
P	-	0.67 (1.03)	-	-
C	0.64 (1.57)	0.25 (1.07)	1.10	1.41
(N, N)	0.88 (1.92)	0.71 (1.63)	1.96	1.44
(C, S)	0.80 (1.76)	-	1.45	1.10
(N, P)	-	0.44 (1.73)	-	-
(P, P)	-	0.19 (1.58)	-	-

The effect of co-doping of anions on the optical absorption spectra (using HSE06 method) of $Sr_2Nb_2O_7$ has been studied. The mono-doping of C, S and co-doping of (N, N) and (C, S) have been considered for describing the double holes mediated coupling. In case of (N, N) doping, the distance between doped N is 1.41 Å, which is very close to the N–N single bond distance of 1.45 Å observed in hydrazine (NH_2–NH_2). This is due to the strong coupling between the partial filled N *2p* orbitals which leads to a bonding and an antibonding state. The optical absorption curves have been calculated using HSE06 method for some mono- and co-doped systems and compared the absorption edge shift with the pure $Sr_2Nb_2O_7$ system which is presented in *Figure 10*. However, considering dopant-dopant coupling, (C, S) and (N, N) exhibit much larger band gap reduction than others. Our study shows that doping of S, (N–N) and (C–S) in $Sr_2Nb_2O_7$ give a reasonable band gap, which can harvest wavelength up to 600 nm of the solar spectrum for efficient photocatalysis.
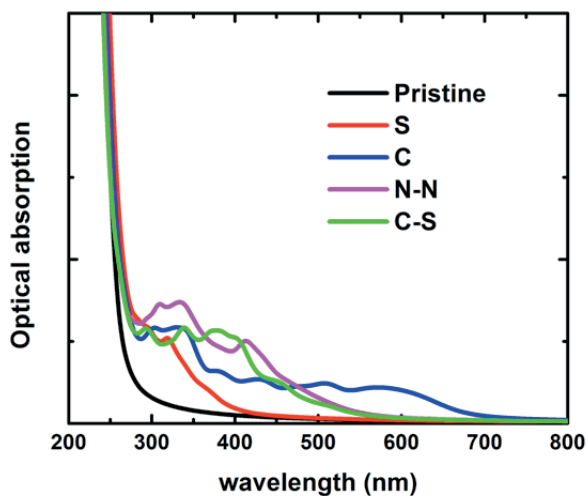
Figure 10. Calculated optical absorption curves (using HSE06 method) of pristine, mono-doped (C and S) and co-doped (N-N and C-S) layered perovskite $Sr_2Nb_2O_7$. Reproduced by permission of the PCCP Owner Societies.

In paper V, the band gap engineering by anionic co-doping in $SrTiO_3$ has been studied for efficient visible-light driven photocatalysis. The relaxed crystal structure of pristine $SrTiO_3$ is presented (*Figure 11*) in which two non-equivalent oxygen sites are labeled as O1 and O2. The non-equivalent oxygen atoms have been substituted by two anionic dopants for the simulation of double holes mediated coupling in $SrTiO_3$. The distance between the two dopant sites is close enough for holes mediated coupling.
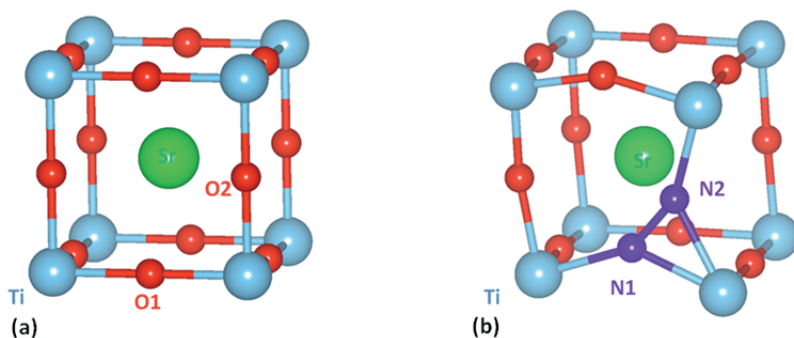
Figure 11. Atomic structures of (a) pure $SrTiO_3$ and (b) anion-anion doped $SrTiO_3$. In (a), the distance between the two O atoms is 2.7 Å. In (b) the N-N bond length is 1.40 Å. Reprinted from the paper V with the permission of the publisher.

The VBM and CBM of the $SrTiO_3$ with different anionic doping combinations have been aligned with respect to reduction and oxidation potential levels. Schematic diagram of VBM and CBM shifting by mono- and co-

doping of anions in SrTiO$_3$ are presented in *Figure 12*. It indicates that doping of N, S, N-N, N-P and P-P in SrTiO$_3$ would be promising materials for the efficient visible-light driven photocatalyst.
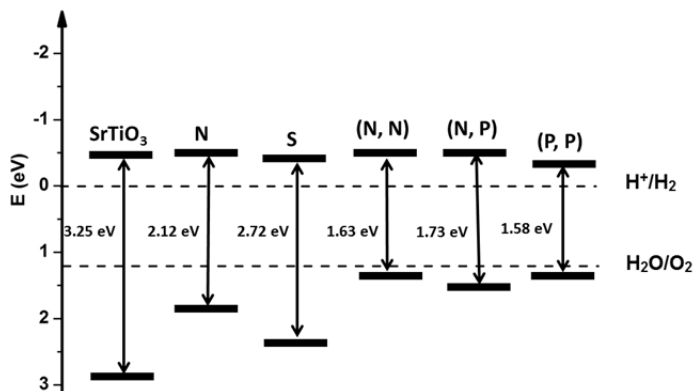

Figure 12. The electronic band edge positions with respect to the water reduction and oxidation potential levels for the pure and doped SrTiO$_3$ systems. Reprinted from the paper V with the permission of the publisher.

3.5.3 Cationic Doping

NaTaO$_3$ has been considered for studying the effect of cations on the electronic structure and optical properties. Recent experimental findings show that two different cations co-doping in the wide band gap semiconductors can increase the photocatalytic activity significantly [79, 80]. Mono-doping of *3d*-transition metal cations are applied to evaluate the effect of dopants on the geometric and electronic structure of NaTaO$_3$ [71]. La doped NaTaO$_3$ system has shown surface nanosteps (*Figure 13*), which increases the surface area and separate the reaction sites that can facilitate the fast rate of reduction and oxidation reactions to increase the photocatalytic activity in the presence of UV light [13, 81, 82]. La mono-doping does not play any role in the band gap reduction but Fe creates some unoccupied states in the forbidden energy gap and increases the visible-light absorption. To achieve high visible-light driven photocatalytic activity of NaTaO$_3$, the strategy of cationic co-doping such as (La, Cr) and (La, Ir) have been demonstrated [83, 84] to achieve the efficient visible-light driven photocatalytic activity.

In paper VI, the effect of mono- and co-doping of La and Fe on the electronic structure of NaTaO$_3$ has been elaborated. The substitution of La at Na site and Fe at Ta site removes the unwanted impurity states which are generated by the Fe mono-doping (*Figure 14*). Therefore, La-Fe co-doping improves the electronic structure of NaTaO$_3$ for solar-driven photocatalysis. The absorption spectra predicted by hybrid functional DFT calculations which well agreed with the experimental findings. The calculated relative

binding energy shows that the co-doped systems are more stable than their respective mono-doped systems. The computational results indicate that doping of Fe and co-doping of La and Fe would reduce the effective band gap of $NaTaO_3$, which would increase the visible light absorption of the photocatalyst.
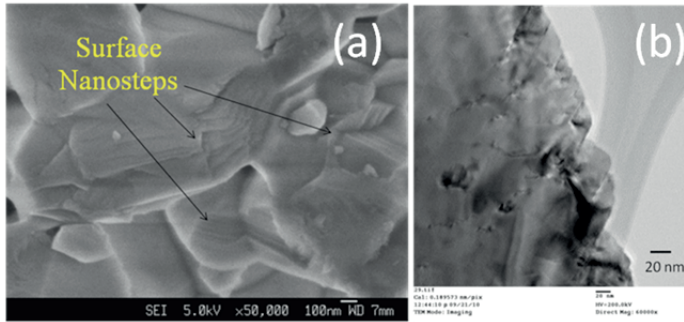

Figure 13. (a) Enlarged view of the surface nanosteps (b) bright field image of 2% La-Fe co-doped $NaTaO_3$.
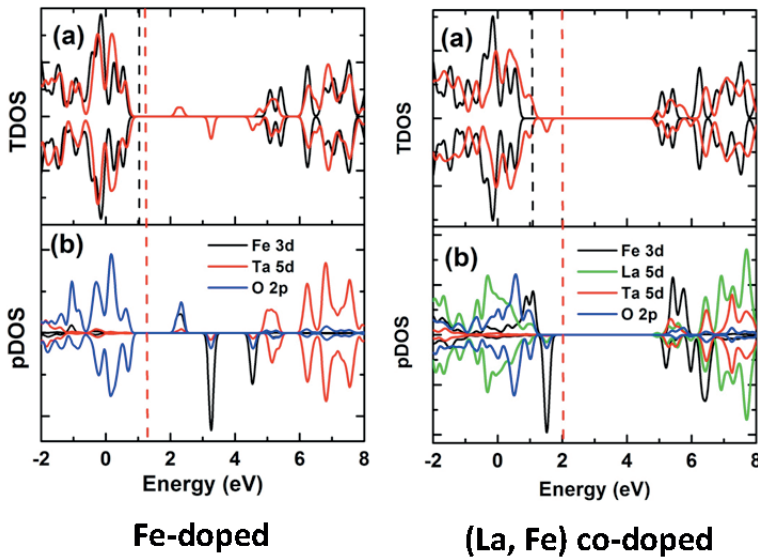

Figure 14. The total and partial density of states (DOS) (using HSE06 method). In pristine $NaTaO_3$ (black lines) and doped (red lines). The vertical dashed lines represent the Fermi energy.

3.5.4 (Anion-Cation) Co-doping

In this thesis, another approach has been developed to improve visible and infrared optical absorption by anion-cation co-doping in wide band gap sem-

iconductors [85]. The layered perovskite $Sr_2Nb_2O_7$ has been considered for the band gap engineering by (anion, cation) co-doping methods. In case of nitrogen mono-doping, the system has one valance electron less than the pristine one, thus a hole is induced. Such holes create an unoccupied state at the top of the valence band edge, which behaves like a recombination center. The effect of nitrogen on the electronic structure of $Sr_2Nb_2O_7$ is illustrated by plotting the total and partial density of states (DOS), which is shown in *Figure 15*a. Electronic structure of N-doped $Sr_2Nb_2O_7$ shows that the Fermi level is pushed towards the valance band edge thus a p-type of semiconductor. It is well known that most cationic doping in metal oxide semiconductors can lower down the CBM significantly. So, Mo has been chosen for the doping at Nb site as they lie in the periodic table very next to each other and their atomic sizes are almost equal. Moreover, the electronic structure of Mo-doped $Sr_2Nb_2O_7$ shows that the Fermi level is pushed close to the conduction band edge, thus resembling to n-type of semiconductor. Filled states are observed at the tail of CBM, which are undesired states for the designing of efficient solar to energy conversion by the photocatalyst. Intermediate states in the band gap can be tuned by choosing different combination and concentration of (p, n) type of dopants. Thus in such cases both the VBM and CBM can be tuned considerably.
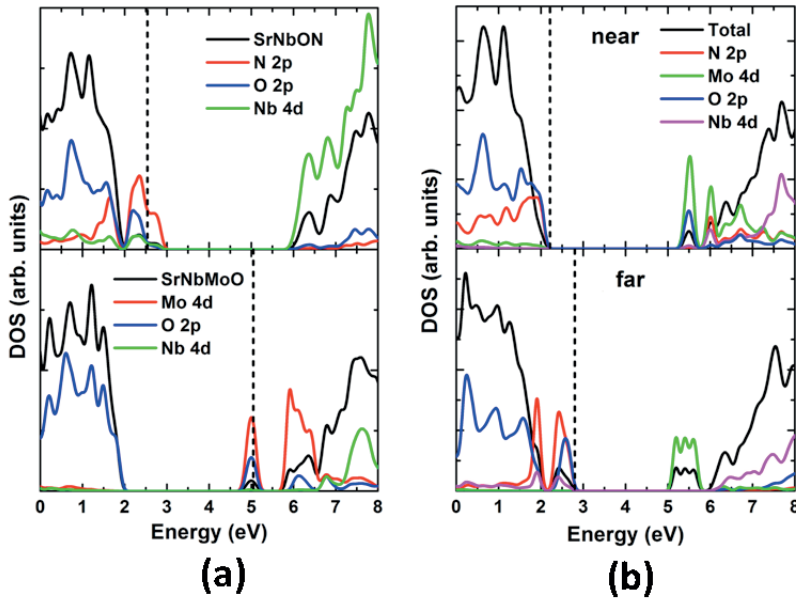

Figure 15. The calculated (using HSE06 functional) total and partial density of states of $Sr_2Nb_2O_7$ with (a) mono doping of nitrogen and molybdenum (b) co-doping with "far" and "near" configurations . The vertical lines indicate the Fermi levels. Reprinted from the paper VII with the permission of the publisher.

To avoid the partial occupied/unoccupied states at the CBM/VBM due to the doping of N or Mo, co-doping of N and Mo in the $Sr_2Nb_2O_7$ have been applied, so that the total number of electrons remains the same as the pristine system. Here, two configurations for the co-doping have been considered, "far" and "near" configuration. The electronic structure of (N, Mo) co-doped $Sr_2Nb_2O_7$ with near and far configurations are presented by plotting the total and partial density of states, which are shown in *Figure 15*b. It is found that band gap reduction is more dominated in case of "far" configuration. The VBM is comprised of the mixing of O *2p* and N *2p* states and the CBM is driven by the continuum-like p-d hybridized states of the O and Mo atoms below the conduction band edge. The calculated binding energies show that (N, Mo) co-doping in $Sr_2Nb_2O_7$ is more stable than their respective mono-doped systems.

In paper VIII, the similar co-doping of (N, Mo) in the $BiNbO_4$ has been applied for the band gap narrowing. The alignment of the valence and the conduction band edges with respect to the redox potential levels, are presented in *Figure 16*. Results show that co-doping of Mo and N in $BiNbO_4$ reduces the band gap up to 31.8%, thus making it a potential candidate for the visible light photocatalysis. The relative stabilities between the mono- and co-doped $BiNbO_4$ materials show that co-doped material is more stable and feasible in comparison to the mono-doped materials.
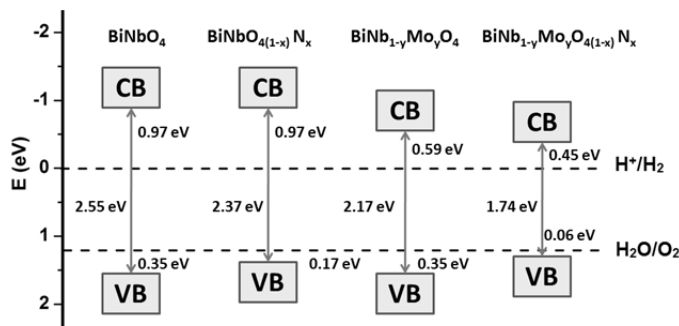

Figure 16. Electronic band edges of $BiNbO_4$ are being aligned with respect to the water reduction (H^+/H_2) and oxidation (H_2O/O_2) potential levels. Reprinted from the paper VIII with the permission of the publisher.

4 Molecular Interaction with Oxide/Nitride Surfaces

4.1 Metal Oxide/Nitride Surfaces

Metal oxide/nitrides surfaces are widely used in various applications such as dissociation of water molecules, cleaning, gas sensing, catalysts etc [86-89]. Dissociation of water on metal oxides surfaces is of fundamental interest for photochemical hydrogen production. Titanium dioxide, silicon nitride and nickel oxide are chosen for water dissociation and gas sensing because of their excellent characteristics such as low cost and high sensitivity. Chemical stability of the metal oxide surfaces at the operation conditions is essentially important for the study the interaction of gas molecules with the surfaces. The coordination number of the metal and oxygen ions at the surfaces is lower than in the bulk. The reactivity of the oxide surfaces arises from low coordination of the surface atoms, which gives rise to unsaturated bonds acting as reactive sites. The oxidation or reduction occurs when the electrons are transferred between the surface and the adsorbates. For an electron acceptor molecule like O_2, n-type semiconductor surfaces (ZnO, SnO_2) are suitable for gas sensing and vice versa. The adsorption behavior of the molecules on the transition metal oxide surfaces is different from that on non-transition metal oxide surfaces because the electrons can be added or removed from d-orbital cations during the chemisorption. Metal oxides, such as TiO_2, ZnO and SnO_2 [90-92] have been widely used for gas sensing materials because of their surface reactivity, high sensitivity, rapid recovery and fast response.

When a surface is formed, the electronic density on and around the surface atoms has been changed due to the dangling bond states. The surface atoms have different charge densities as compared to the bulk atoms. As a result, the surface is reconstructed. Generally, surfaces with a smaller reduction in its coordination number with respect to that of its bulk show higher stability. The transition metal oxides contain positively charged metal cations and negatively charged oxygen anions. If a surface contains both types of ions (anion or cation), it is called a polar surface. But it is difficult to construct polar surfaces due to their instability. Molecular adsorption on the surfaces can be distinguished into two types: physisorption and chemisorption [93]. In case of physisorption, adsorbates are bound to the surfaces very

weakly due to the van der Waals attractive forces and this interaction does affect the electronic structure of the substrate. Physisorption is characterized by low binding energies on the order of 0.01-0.15 eV and equilibrium separation is around 3-10 Å. In chemisorption, strong ionic or covalent bond is established between the molecule and metal oxide surface, which strongly affects the charge exchange mechanism. The binding energies are very high, in the order of couples of eV and equilibrium separation between the molecule and the surfaces are about 1-3 Å. The electronic structure of the adsorbed system is changed due to the charge transfer between the highest occupied molecular orbital (HOMO) of surface and the lowest unoccupied molecular orbital (LUMO) of the adsorbed molecule, respectively and vice versa. When the surface coverage is around 1ML, the lateral interaction between the molecules (van der waals attraction and dipole-dipole forces between adsorbates) is more significant as compared to that at low coverage.

This chapter is devoted to the study of the interaction of metal oxide/nitride surfaces with gas molecules such as H_2O, SO_2, NH_3, NO_2, H_2S. In this thesis, the systems that are discussed are (i) interaction of water molecules with the surfaces of rutile TiO_2 nanowire and β-Si_3N_4 (0001) surface for the dissociation of water molecule; (ii) Adsorption of SO_2 on the anatase TiO_2 (001) and (101) surfaces; and (iii) Adsorption of different gas molecules such as NH_3, NO_2 and H_2S on the NiO (100) surface for gas sensing application. Surface states due to dangling bonds or defects are identified and their relation with geometrical structure of the surface as well as their modification by molecular adsorption. Concentration of unoccupied states or reduction of band gap has been increased by the rising the molecular coverage which gives the high electronic conductivity which is the gas detecting parameter.

4.2 Dissociation of Water Molecules on Surfaces

The atomistic mechanism of splitting of water molecule by the reactive metal oxide/nitride surfaces is investigated by using *ab-initio* calculations in the context of clean energy [94-96] generation. Understanding of water/solid interfaces has crucial importance for H_2 production via dissociation of water, corrosion, catalysis and mineralogy. Water is impossible to exclude from realistic environments. Extensive research on the reactions of water on metal oxide surfaces have been performed for the discovery of photochemical water splitting. Oxide surfaces can oxidize the water molecules which dissociates into H and OH group on the surface [97, 98].

44

4.2.1 Rutile TiO$_2$ Nanowire

We have employed the DFT simulation to describe the effect of point defects on the water interaction with the different surfaces of TiO$_2$ nanowire. Since the binding of surface atoms are weaker than that of the bulk atoms it would cost comparatively less energy to remove them from the system to create point defects. Surface defects such as anionic or cationic vacancies strongly influence the chemistry of metal oxide surfaces. Stronger adsorption of molecules occurs at steps and defective sites, which can often dissociate the molecules. In the case of the O-vacancy on the transition metal oxide surfaces, the population of the *d*-orbital electrons on neighboring cations increases due to the local charge neutrality. These cations act as reactive sites for the chemisorption or dissociation of molecules. In paper IX, the possible intrinsic defects on the surfaces of rutile TiO$_2$ nanowire have been studied. Defect formation energy, 0.145 eV/f.u at O-rich condition is suitable for the easy creation of O-vacancy and O-poor condition is favorable to create Ti vacancies with formation energy, 0.263 eV/f.u at the TiO$_2$ nanowire surfaces.
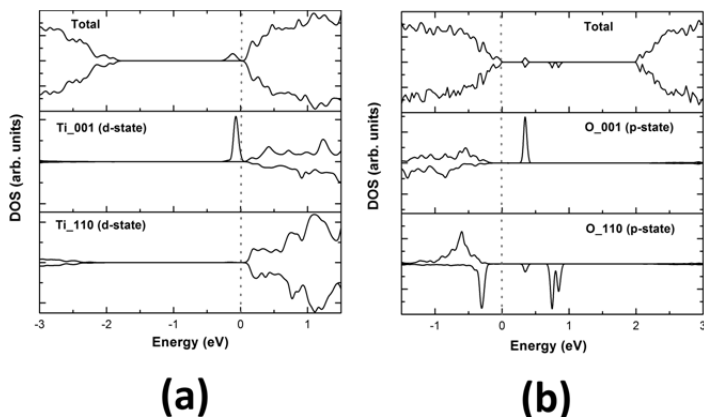
Figure 17. Total and partial DOS of rutile TiO$_2$ nanowire with defects (a) O-vacancy and (b) Ti-vacancy. Reprinted from the paper IX with the permission of the publisher.

In paper IX, the effect of defects (anion or cation vacancy) on the electronic structure of rutile TiO$_2$ nanowire is evaluated by plotting the total and partial density of states (*Figure 17*). It indicates that the O-vacancy introduces n-type states in the band gap of nanowire. The occupied defect states appear at the edge of the CB, which is due to the polarization of neighboring Ti atoms. These electronic states may enhance the charge transfer process between surface and adsorbent molecule. The O-deficient system contains an excess of electrons, which form a triplet state and unpaired electrons are localized on the Ti atoms adjacent to the O-vacant site. So in the case of an O-vacancy, neighboring Ti atom behaves as reactive site for the adsorption

of molecules. In the case of Ti-vacancy, unoccupied defect states of p-type appear in the band gap where the lower one is about 0.28 eV above the edge of VB. These states in the band gap are due to the polarized holes of neighboring O atoms.

The detailed understanding of water interaction with the surfaces of TiO_2 has become one of the leading topics in the area of oxide surface chemistry. Molecular adsorption on metal oxide surfaces have been investigated on the basis of the adsorption energies, preferential adsorption sites, charge transfer mechanism as well as from electronic and structural perspectives. The most reactive sites for water dissociation on metal oxides are the defective sites [99]. In paper IX, interaction of water molecules with perfect or defective (V_O and V_{Ti}) surfaces of rutile TiO_2 nanowire have been investigated. Dissociation of water molecule is not observed on the surfaces of perfect and V_{Ti} nanowire. The average adsorption energies per water molecule are 0.85, 1.63 and 0.29 eV/f.u for perfect, V_O and V_{Ti} systems, respectively. But the water molecule undergoes spontaneous dissociation on the (001) surface of the nanowire with V_O defects. The charge transfer mechanism is explained from an analysis of charge distribution with and without the adsorption of water molecules on the surface with O-vacancy (*Figure 18*). The adsorbed water molecule is dissociated into H and OH at the surfaces with O-vacancies. The hydrogen atom attaches to the surface O-site forming OH unit, while the remaining hydroxyl unit (OH) stays bound to Ti atoms. This is due to the transfer of charge from Ti to O atom of adsorbed water molecule. Such spontaneous dissociation indicates that there might be a small activation barrier for this process. Water dissociation on metal oxide surfaces is reversible, because the dissociation products could be heated to form water molecule. To avoid the recombination of water, strong binding between the oxygen of water and cation site of the surface is required, which is provided by the defects such as the O-vacancy.
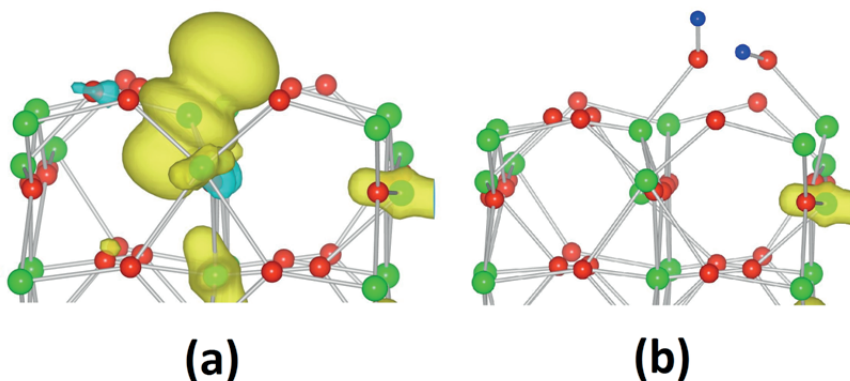

(a)   (b)

Figure 18. Partial charge density distribution of Ti atom at the TiO_2 (001) surface of nanowire with O-vacancy, (a) without the adsorption of H_2O molecule (b) with H_2O molecule. Reprinted from the paper IX with the permission of the publisher.

4.2.2 β-Si$_3$N$_4$ (0001) Surface

In paper X, the variation in the structure, energetic and electronic properties of the β-Si$_3$N$_4$ (0001)-surface with the adsorption of water molecules have been investigated for the elucidation of the dissociation mechanism. The surface states are found to be more localized on top of the valence band and at the bottom of the conduction band for the clean β-Si$_3$N$_4$ (0001)-surface. Furthermore, unoccupied states appear in the band gap, due to dangling bonds at the atomic sites with lower coordination (3c-Si and 2c-N), which serve as reactive sites for the dissociation of water molecules. For water interaction, at 0.5 coverage, all water molecules undergo dissociation (OH–H) where the hydrogen atoms attach to N (2c) sites forming NH units, while the remaining hydroxyl units (OH) remains bound to Si (3c) atoms. Chemisorption mainly occurs on atoms with lower coordination number. When these sites are saturated with adsorbates, additional H$_2$O molecules do not get to dissociate on them and thereby form a second ad-layer (physisorption process). So in case of full coverage, half of the adsorbed water molecules are dissociated, which is in good agreement with the experimental findings [100]. The water adsorption on β-Si$_3$N$_4$ (0001)-surface is found to be an exothermic process with 2.72 eV/H$_2$O mol. being the average dissociation energy of chemisorbed water molecules. It is found that surface electronic states decrease in the band gap by increasing coverage because the dissociated molecules make new bonds with the surface atoms.

4.3 Adsorption of Gas Molecules

Many hazardous gases such as NH$_3$, SO$_2$, NO$_2$ and H$_2$S are atmospheric pollutants, which are produced from the industries and coal/oil burning. Sensing these toxic gases is very crucial to achieve a clean environment. Solid-state gas sensors are established due to their high sensitivity and low production cost. Oxidizing or reducing of gases on the surfaces of metal oxides can be conveniently detected by calculating the conductivity of the gas sensing materials.

4.3.1 Anatase TiO$_2$ Surfaces

In paper XI, the O-vacancy on the anatase TiO$_2$ (101)- and (001)-surfaces have been studied for the adsorption of SO$_2$. According to the defect formation energies, O-poor conditions are suitable for the easy creation of O-vacancies at the anatase TiO$_2$ surfaces. To maintain the charge neutrality on the surfaces, neighboring Ti atoms are polarized due to the Ti *3d* states whose electronic charge distribution is shown in *Figure 19*. Ti-atoms are affected directly by the creation of an O-vacancy, and are then polarized by a

magnetic moment of about 0.5 μ_B, while, the unaffected Ti-atoms are polarized with a very small magnetic moment. According to the Bader analysis [101] of electronic charge distribution, the charge on each of the two Ti atoms neighboring to the O-vacant site is -0.22e, implying that some additional electronic charge is localized on these Ti atoms. It is found that electronic states associated with the defects appear at the bottom of conduction band, which may enhance the charge transfer between the surface and gas molecule.
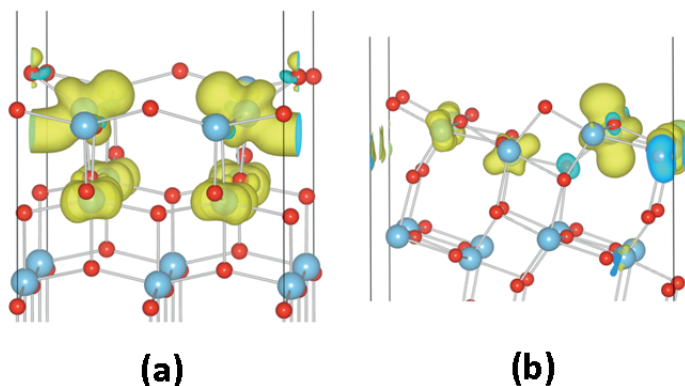
Figure 19. Partial charge distribution of anatase TiO_2 with O-vacancy (a) (001) surface (b) (101) surface.

The interaction of sulfur dioxide with both nearly perfect and defective anatase TiO_2 (101)- and (001)-surfaces have been studied. . It signifies that no SO_2 molecules are found to be absorbed on defect free surfaces, which is confirmed by the experimental results. Experimentally, it is found that sulfur is weakly bound on the TiO_2 films with S^{4+} oxidation state at room temperature (298 K) and without UV irradiation. Adsorption of an SO_2 molecule on anatase TiO_2-surfaces with an O-vacancy is found to be an exothermic process with adsorption energies, 2.79 and 1.73 eV, respectively. The reactivity of the surfaces is enhanced by the formation of defects (O-vacancy) induced by the irradiation of UV light and also by the rise in temperature of the system. It implies that the SO_2 molecule on the surfaces heals the Ti atoms affected by the O-vacancy. The SO_2 molecule strongly binds to the defective sites on the surfaces via a chemisorption process, which is indicated by the charge transfer mechanism. The strong transfer of charge from Ti to S via O stabilizes the Ti-O bond, which shows up as strong adsorption on the surfaces with O-vacancies. In *Figure 20,* isosurface of differential charge density clearly indicates the charge depletion and accumulation between the surface Ti atoms and SO_2 molecule.

According to the Bader analysis, S atom gains 1.1e and 1.0e electronic charge from the neighboring Ti atoms, thereby reducing its oxidation state

of S is +3 by the adsorption of SO_2 on TiO_2 (001)- and (101)-surfaces at the defective sites. For further elaboration the effect of chemisorption on the electronic structure have been investigated, it is found that the peak appearing below the conduction band is contributed by the S $3p$ and Os $2p$ and separated from CBM. In case of TiO (001)-surface, the valence band is slightly shifted upwards by 0.11 eV as compared to the clean surface but in (101) surface, occupied states have merged with the conduction band. It implies that the adsorption of SO_2 molecules on such defective surfaces heals the Ti atoms affected by the O-vacancy.
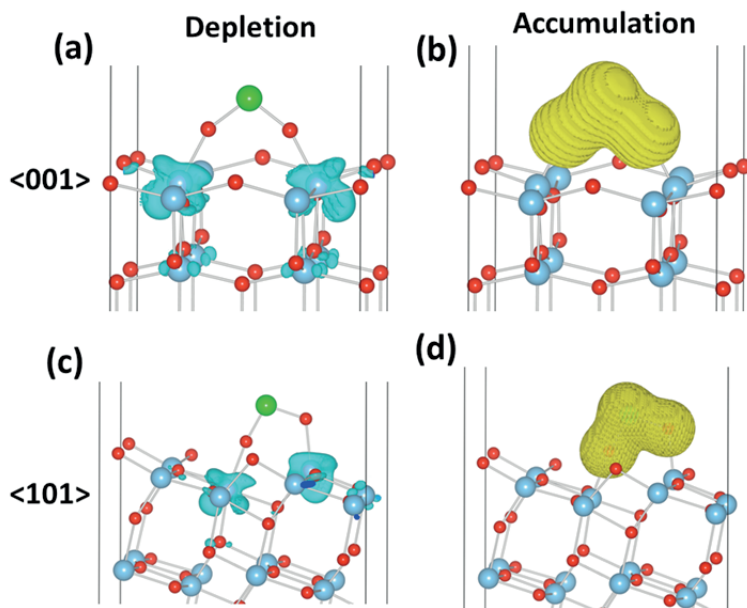
Figure 20. Isosurfaces of differential charge density (yellow-accumulation, cyan-depletion) The differential charge density is obtained by:

.

A humid and oxygen-rich ambience is commonly encountered in experiments, which needs to be realistically considered in our model studies. In the formation of SO_3 and SO_4 radicals, S atom loses its electrons to the more electronegative O atoms. In SO_4, the oxidation state of S attains +6, as given out by the Bader analysis of electronic charge. Therefore, the ease in the formation of SO_4 is enhanced with the rise in temperature and intensity of UV radiation which is in good agreement with the FTIR absorption spectra.

4.3.2 The NiO (100) Surface

Nickel oxide (NiO) is considered as model p-type metal oxide material due to its good chemical stability and suitable electronic properties. The magnetic ordering in the (100)-surface is antiferromagnetic [102, 103]. Two well separated sub-bands of the e_g states appear in case of the NiO (100)-surface. The peak at the conduction band edge is contributed by d_{z^2} states, which is only subject to the field generated by the oxygen atoms below the Ni surface atom. While the crystal field felt by the $d_{x^2-y^2}$ orbital does not change the electronic structure as compared to the bulk structure. The reason behind it is that the band gap of the surface is smaller than that of the bulk. The mechanism of gas sensing is related to absorption of the gas molecules on the sensors surface with changes of the conductivity of the thin films. In this study, the DFT+U method has been employed to study the electronic properties and gas sensing mechanism of NiO. The adsorption of H_2S, NH_3 and NO_2 molecules on the NiO surfaces has been investigated. Trend of adsorption energies of gas molecules with different coverage are shown in *Figure 21*. Due to the interaction between the gas molecules and the NiO (100)-surface, electronic structure of the adsorbed system has been changed with respect to the bare NiO surface. One, two, and four molecules absorb to the NiO (100)-surface which correspond to 0.25, 0.5 and 1 ML coverage for molecular adsorption.
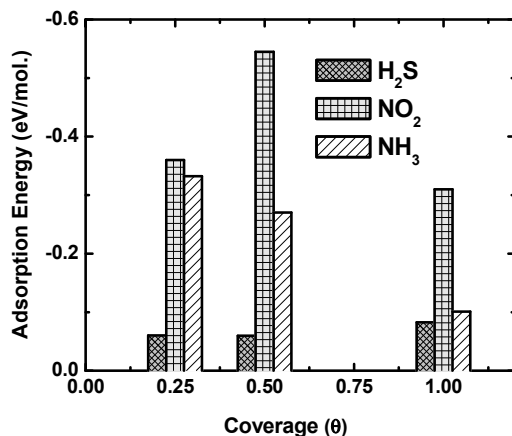
Figure 21. Adsorption energies per H_2S, NO_2 and NH_3 gas molecules on NiO (100) surface with different coverage.

The H_2S and NO_2 molecules are planar and were therefore put perpendicular to the surface plane with S atom and N atom close to the surface, while the NH_3 molecule was put onto the surface with the N atom close to the surface. Adsorption of the H_2S molecule on NiO (100)-surface is energetically

favorable for all coverages and the adsorption energies per molecule are 0.060, 0.059 and 0.082 eV for 0.25, 0.5 and 1 ML coverage, respectively. The change of electronic structure of the NiO (100)-surface with different adsorbed gas molecules have been investigated by plotting the total density of states (TDOS) shown in *Figure 22*. It is observed that the band gap of NiO (100) is reduced upon the adsorption of H_2S gas molecules by 0.06 and 0.16 with corresponding to coverage of 0.25 and 0.5 ML, respectively, which is the main parameter to detect the gas molecules. At 1ML, H_2S molecules interact with each other instead of NiO surface, thus electronic structure is not changed.
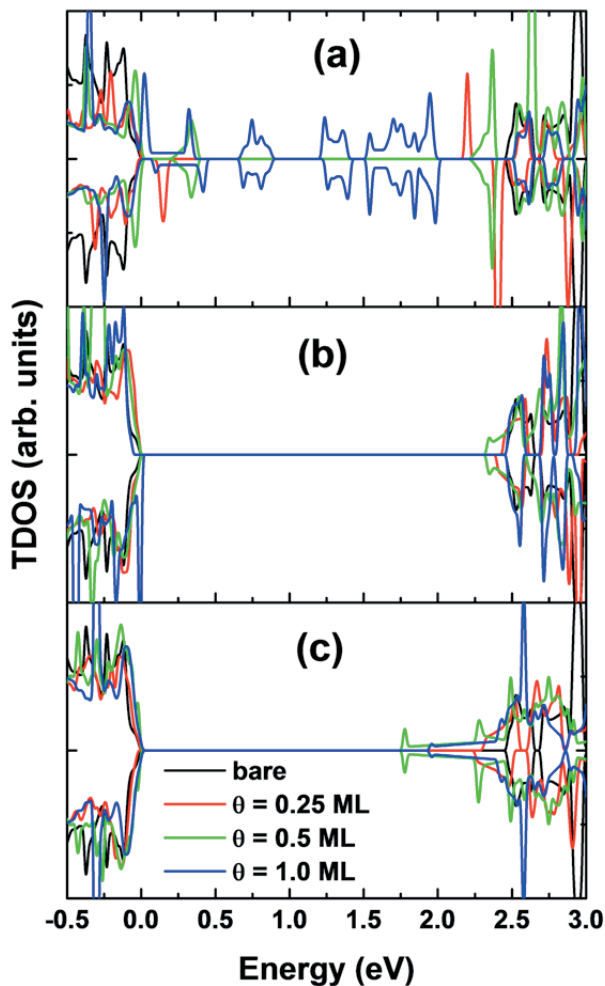
Figure 22. Total density of states (TDOS) of NiO (100) surface with the adsorption of (a) NO_2, (b) H_2S and (c) NH_3 and NO_2 for the different coverage using GGA+U method.

For the adsorption of the NH_3 molecule, the stable adsorption site is on top of the Ni atom. Adsorption energies were found to be -0.33, -0.27 and -0.10 eV per NH_3 molecule for 0.25, 0.5 and 1 ML coverage, respectively (shown in *Figure 21*). The band gap is found to decrease with the adsorption of NH_3 molecules at different coverage, which indicates that conductivity of NiO surface increases upon its exposure to NH_3 gas. But the band gap reduction does not vary linearly with the coverage of gas molecules on the surface. Similarly, the adsorption of NO_2 gas molecules on the NiO (100)-surface has been investigated, the adsorption energy of NO_2 is found to be higher as compared to the other gas molecules. The stronger interactions of the NO_2 gas with the surface lowers the sensor response since the removal of the adsorbed molecules become more difficult which is in good agreement with previous experimental result [104]. *Figure 22* shows that at low coverage (0.25 ML) band gap is reduced drastically, and NiO (100)-surface shows metallic behavior at high coverage.

Charge transfer between the gas molecule and the surface has been investigated by the Bader analysis. To understand the bonding mechanism of gas molecules at NiO (100)-surface, electron density difference, $\Delta\rho = \rho_{(NiO:mol)} - (\rho_{NiO} + \rho_{mol})$ is calculated which illustrates how the charge density changes during this adsorption process. Figure 23 shows the isosurfaces of differential charge density of the NO_2, H_2S and NH_3 molecules adsorbed on NiO (100) surface. Here the charge density can be either positive (depletion) or negative (accumulation) depending on whether an atom gains or loses charge.

(a) **(b)** **(c)**
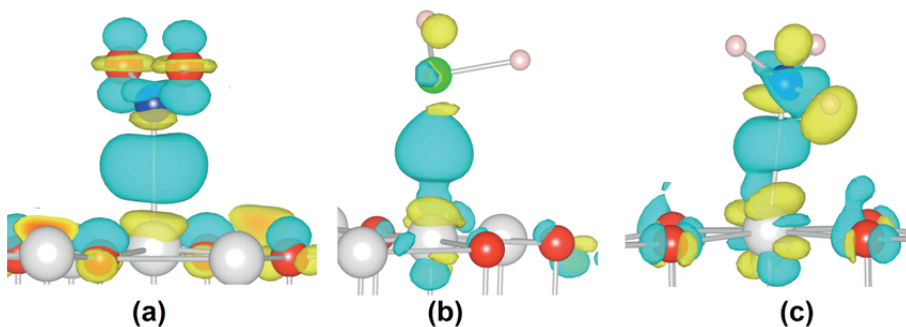
Figure 23. Isosurface of differential charge density of (a) NO_2, (b) H_2S and (c) NH_3 gas molecule adsorbed at NiO (100) surface (yellow-depletion, cyan-accumulation).

5 Electronic Structure of Kaolinite

Clay minerals are abundant all over the earth and impact a wide variety of disciplines such as environmental chemistry, drug delivery, geology and the ceramics industry. Clays are also used for the underground storage sites for high-activity radioactive waste due to their low permeability to water and high retention capacity for cations. Normally, natural kaolinite contains impurities such as iron, magnesium, alkali metals, alkaline earths and other cations [105]. The crystal structure and electronic properties of clay mineral surfaces are still far from the complete atomic level, and lags behind the existing knowledge of other complex metal oxides. The amount and position of the intrinsic or extrinsic defects inside the crystal plays an important role for the mechanical, thermal, electrical, and optical properties of kaolinite. An accurate interpretation of the electronic structure by means of spectroscopy data and first-principles calculations at an atomic scale is very important for many industrial applications.

5.1 Crystal Structure

Kaolinite ($Al_2Si_2O_5(OH)_4$) is a two-layered aluminosilicate, which forms the triclinic structure (space group P1) at ambient conditions [106], forms thin platy stacked clusters of pseudohexagonal sheets in thick books which are observed in the SEM micrographs. The number of plates and the plate diameters in the stacks are different for natural and synthetic kaolinite, which might be related to the fact that natural kaolinite is more prone to defects than synthetic kaolinite. A single layer of silica tetrahedra is connected by common apex oxygen atoms to a single layer of alumina octahedra, thus making a 1:1 phyllosilicate, crystal structure of pristine kaolinite, shown in *Figure 24*. Most of the hydroxyl (OH) groups are located on the aluminate-terminated (0 0 1)-surface. In order to elucidate its mechanical, thermal, electrical, and optical properties for industrial applications, a proper description of the electron band structure is of critical importance.
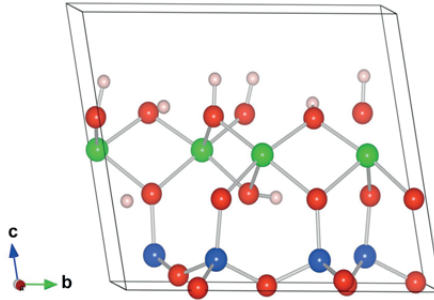
Figure 24. Crystal structure of pristine kaolinite: Here, Si, Al, O, and H are represented by blue, green, red, and white spheres, respectively. Reprinted from the paper XIII with the permission of the publisher.

5.2   The electronic Structure of Pristine Kaolinite

The electronic structure of pristine kaolinite has been studied, using the stat of the art methods to estimate the band gap. The calculated band gap of the pristine kaolinite is 4.9, 6.2 and 8.2 eV with the GGA-PBE, HSE06 and GW approach. The estimated band gap of kaolinite is therefore estimated as between 6.2 and 8.2 eV. This result is in qualitative agreement with previous results [107], which expect the band gap of kaolinite to be close to that of Al_2O_3. The total and partial density of states of kaolinite is plotted (*Figure 25*). It is found that the VB mainly comprises O *2p* states, whereas the CB possesses *3p* states of Si and Al.
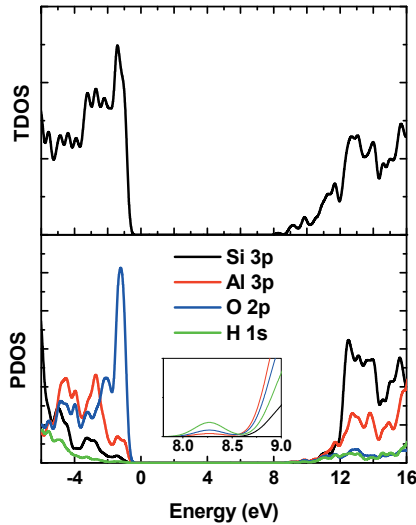
Figure 25. Total and partial density of state of pristine kaolinite using state-of-art method (GW approximation); The Fermi level is set at zero.

5.3 Defect Formation Energy

Physical and chemical properties of kaolinite may be fundamentally changed by the presence of intrinsic defects. The electronic structure of kaolinite is affected by intrinsic defects, which may behave like trap sites for electrons or holes. The kaolinite (001)-surface is the main exposed surface, [108] so we assumed that the possibility of defects is higher on this surface. Therefore, the intrinsic defects situated on the (001) surface have been considered. Here, four different types of defects are investigated: H-vacancy (V_H), OH-vacancy (V_{OH}), both H and OH vacancy ($V_H V_{OH}$), and the replacement of an H atom by an oxygen (O_H). The atomic potentials are variable and can be controlled by the experimental conditions. In order to understand the favorable kind of defects, the defect formation energies have been calculated at five environmental chemical growth conditions, which are listed below:

A (Si-, Al-poor, O-rich, H-poor)
B (Si-, Al-poor, O-rich, H-rich)
C (Si-, Al-rich, O-poor, H-rich)
D (Si-, Al-rich, O-rich, H-poor, H_2O restricts the H chemical potential)
E (Si-, Al-rich, O-poor, H-rich, H_2O restricts the H chemical potential)

   The neutral point defect formation energy of the above mention defects at different chemical growth conditions are presented in *Figure 26*.
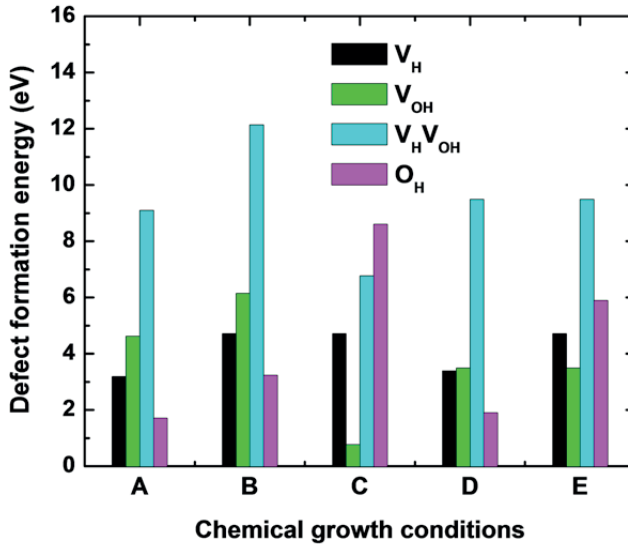
Figure 26. Defect formation energy of different neutral native point defects in kaolinite at different growth conditions.

5.4 Defect States in Kaolinite

Knowledge of the local structural and electronic properties of these defects is required for the reliable understanding of experimental measurements. In paper XIII, the effect of intrinsic defects on the electronic structure of kaolinite has been investigated using GGA-PBE, HSE06 and GW methods. In case of V_H, $V_H V_{OH}$ and O_H defects, unoccupied defect states appear at the upper edge of the VB and it behaves as a shallow acceptor. The finite density of states at the Fermi level allows for shakeup transitions from states just below the Fermi level to empty states just above the Fermi level at elevated temperatures. The shape of the conduction band of kaolinite with these defects is not changed. But the V_{OH} creates filled impurity states at the bottom of CB shifting the Fermi level is shifted to the CB. It shows that V_{OH} in kaolinite behaves as a shallow donor in the material. Our hope is that first-principles results provide guidance for understanding the physical, chemical and electronic properties of intrinsic defects in kaolinite.
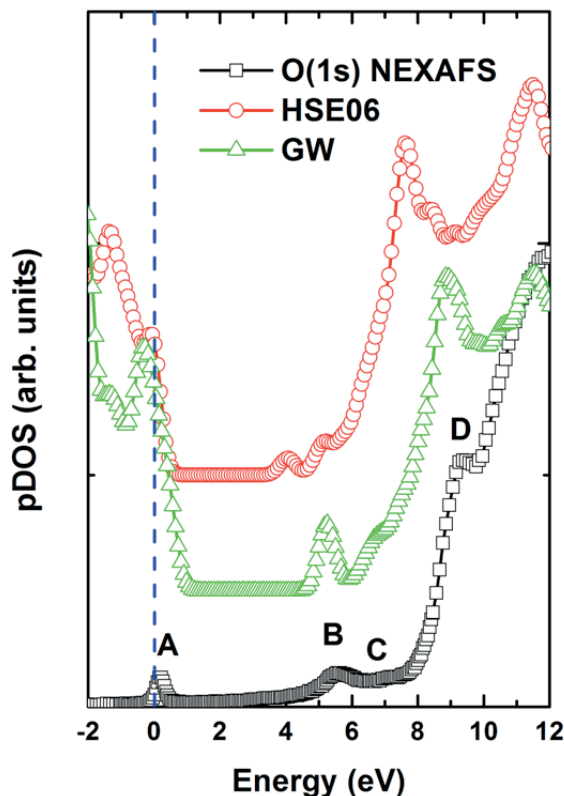
Figure 27. pDOS of O *2p* states of the kaolinite with O_H defect including core hole effect on oxygen atom using HSE06 and GW approximation which is compared with the experimental NEXAFS data.

In order to evaluate the electronic structure of natural kaolinite, the soft x-ray spectroscopic techniques Near Edge X-ray Absorption Fine Structure (NEXAFS) along with state-of-art first-principle calculations have been applied. The calculated defect formation energy (*Figure 26*), it indicates that O_H has lower formation energy at O-rich growth condition than the other defects using GGA-PBE and HSE06 calculations, which indicates that the probability of creating O_H defects in kaolinite is much higher than creating other defects at these conditions. To simulate the NEXAFS data, the core-hole effect on the different oxygen atoms has been involved by the Z+1 approximation [52], assuming equal probability to form a core hole at oxygen site and took the average of the pDOS of the oxygen atoms with the core hole (*Figure 27*). The Peak at 526.3 eV in the NEXAFS spectrum was aligned to the Fermi level of the oxygen *2p*. The shape of the NEXAFS spectrum closely resembles the O *2p* pDOS calculated by using hybrid function (HSE06) method and GW approximation but HSE06 slightly underestimates the optical band gap.

The calculated (GW approximation) energy the energy difference between the peaks (A, B), (B, C) and (C, D) are 5.26, 1.41, and 2.17 eV, respectively which correlates well with O 1s NEXAFS (5.53 eV, 1.31 eV and 2.44 eV). From our results, it is concluded that peak A (just above the Fermi level) is due to the O_H defect (O-O pair) and the main cause of the second peak at B is the core hole effect on the different oxygen of kaolinite. According to the pDOS of O-H bonds, it is observed that feature B, C and D are found to be a sum of the DOS of all O-H bonds in the kaolinite when core hole are applied at the oxygen atoms which are located inside the kaolinite sheet. It is proposed that natural kaolinite, being more prone to defects than synthetic displays different intensity at C and D peaks as compared to synthetic kaolinite because the relative decrease of the O-H bonds in the natural kaolinite as they are replaced by O-O pairs.

6 Conclusions and Outlook

In this thesis, the state-of-art calculations have been performed to investigate the atomic-scale design of photocatalysts for hydrogen production, dissociation of water at reactive metal oxide surfaces and the electronic structure of kaolinite materials.

The photocatalyst designing is being investigated by the possibility of converting UV to visible active photocatalyst by their band gap engineering. A number of UV light active photocatalysts such as $Sr_2Nb_2O_7$, $BiTaO_4$, $BiNbO_4$, $SrTiO_3$ and $NaTaO_3$ have been studied for their band gap narrowing to harvest the visible region of solar light by the cationic and anionic doping. It is found that the lowered band gap does not guarantee to improve the H_2 evolution efficiency and band positions are also very important. Therefore, the choice of dopants is very crucial part for efficient solar-active photocatalyst. Anions (S, N, C, P) and cations (Mo, Fe, La) have been applied in the above mentioned materials for narrowing the band gap. The mono anionic (N, S, P, C) doping in $Sr_2Nb_2O_7$, $BiTaO_4$ and $SrTiO_3$ reduce the band gap by the shifting of VBM upward but it creates occupied or unoccupied states in the band gap which behave as recombination centers. To avoid these unwanted states, (anion, anion) co-doping has been considered for band gap narrowing by the double holes mediated coupling between two anion dopants which can narrow the band gap significantly. It is proposed that (N, N) and (C, S) co-doped layered perovskite $Sr_2Nb_2O_7$ is promising material for visible-light driven photocatalyst. The electronic structure and the optical absorption spectra indicate that co-doping of (N, N), (N, P) and (P, P) in $SrTiO_3$ improve the visible-light harvesting for efficient photocatalysts.

It is revealed that Fe-doped $NaTaO_3$ creates unoccupied states in the band gap to increase the visible-light absorption but these intermediate states behave as recombination centers. Doping of La does not effect on the electronic structure of $NaTaO_3$ but create nanostep on surface. The (La, Fe) co-doped $NaTaO_3$ not only increase the surface area of sample but also narrows the band gap in the visible-light region. It is concluded that (La, Fe) doping increase the hydrogen production efficiency in the presence of visible-light based on our theoretical and experimental findings.

In this thesis, the electronic structures of (N, Mo) co-doped $Sr_2Nb_2O_7$ and $BiNbO_4$ systems have been studied and their electronic band positions are aligned with respect to the water redox levels. Co-doping of N and Mo in $Sr_2Nb_2O_7$ is found to be an excellent combination for visible-light active

photocatalyst with respective band gap 2.14 and 2.94 eV for "far" and "near" configurations, respectively. It is also concluded that the relative stability of co-doping is more stable as compared to the respective mono-doping.

The metal oxide/nitride surfaces such as TiO_2, NiO and β-Si_3N_4 have been investigated for dissociation of water molecule and adsorption of gas molecules (SO_2, NH_3, NO_2 and H_2S) for gas sensing. Water adsorption is shown to be dissociative at the O-deficient (001)-surface of rutile TiO_2 nanowire because of the charge transfer from the surface Ti atom to the water molecule. Our results show a possible explanation for the spontaneous dissociation of water molecules on TiO_2 and β-Si_3N_4-(0001). The defects are involved in the adsorption process of sulfur dioxide molecules at the TiO_2 (101)- and (001)-surfaces, which are also confirmed by the Fourier transform infrared (FTIR) spectra. Fixation of SO_2 molecules on TiO_2 surfaces has explained electronic structure and change in oxidation state of sulfur by charge transfer. NiO has been proposed as good candidate for gas sensing of many hazard gases such as NO_2, H_2S and NH_3. Chemisorption interaction of NO_2 molecule with NiO surface is very strong as compared to the H_2S and NH_3 molecules and contributes extra peaks within the band gap. H_2S molecules weakly interact with the NiO (100)-surface and the band gap slightly decrease with the increase of coverage up to 0.5 ML. In case of NH_3 molecular adsorption, the adsorption energy has been increased with the increase of coverage and the band gap is directly related to the adsorption energy. Charge transfer mechanism between the gas molecules and the NiO surface has been illustrated by the Bader analysis and plotting isosurface charge distribution.

In the last part of thesis the electronic structure of kaolinite with many possible defects has been studied by theoretical simulation and has been compared with their experimental findings. The accurate optical band gap of kaolinite has been predicted and simulates the effect of different possible defects on their electronic structure. The calculated band of defect-free kaolinite is estimated between 6.2 and 8.2 eV using different computation methods. It is found that the presence of defects creates the p-type or n-type impurity states in the band gap. It is observed that O_H defect has lower formation energy as compared to the other defects at O-rich growth condition, which indicates that the probability of this defect is higher than others. The theoretical GW approach gives the good estimation of the electronic structure of kaolinite, including defects and core hole effect, which provides an accurate description of NEXAFS spectra.

7   Sammanfattning

I den här avhandlingen har första princip-beräkningar utförts för att undersöka tre olika huvudområden: Atomistisk design av fotokatalysatorer, dissociering av vatten på reaktiva metalloxid ytor och elektronstrukturen för kaolinitlera.

Inom området fotokatalytisk design har möjligheten att påverka band gapet hos ett material så att dess fotoaktiva område försjuts från UV-regimen till synligt ljus. Material såsom $Sr_2Nb_2O_7$, $BiTaO_4$, $BiNbO_4$, $SrTiO_3$ and $NaTaO_3$ har studerats för att förskjuta deras aktiva regim till synligt ljus med hjälp av katjon- och anjondopning. Vi har funnit att ett minskat bandgap inte nödvändigtvis garanterar en effektivare vätgasutveckling och att lingeringen av bandkanter är av stor betydelse. Därför är valet av dopatomer mycket avgörande för att erålla en effektiv fotokatalysator inom det synliga området, Anjoner (S, N, C, P) and katjoner (Mo, Fe, La) har använts som dopatomer för att minska bandgapet. Dopning med enbart anjoner i $Sr_2Nb_2O_7$, $BiTaO_4$ och $SrTiO_3$ reducerar bandgapet och förskjuter valensbandmaximat till högre energier, men skapar också tomma och fyllda tillstånd vilka agerar som så kallade rekombinationscentra. För att undvika dessa oönskade tillstånd, så har (anjon-anjon)-dopning undersökt. Så kallad Dubbelhål-medierad koppling mellan två anjoner fanns minska bandgapet betydligt. Vi föreslår att en (N, N) och (C, S)-dopad lagerstruktur av perovskit $Sr_2Nb_2O_7$ är ett lovande material för en solljusdriven fotokatalysator. Elektronstrukturen och absorptionsspektra indikerar att dopning med (N, N), (N, P) and (P, P) in $SrTiO_3$ förbättrar absorptionen av synligt ljus, vilket öppnar för en effektiv fotokatalys. Vi har också funnit att Fe-dopad $NaTaO_3$ skapar tomma tillstånd i bandgapet. Dopningen ger högre fotoabsorption, men tillstånden uppför sig också som rekombinationscenter. Dopning med La påverkar inte bara $NaTaO_3$'s elektronstruktur, utan skapar också, nano men skapar ochså nanosteg på ytan. (La, Fe)-dopad $NaTaO_3$ ökar dels ytarean, visar sig också minska bandgapet inom synliga området. Från detta kan slutsatsen dras att (La, Fe)-dopning ökar effektiviteten vid väteproduktion.

Elektronstrukturen för (N, Mo)-dopad $Sr_2Nb_2O_7$ och $BiNbO_4$ har studerats och bandkanterna har linjerats med avseende på redoxpotentialerna för vatten. Dopning av N och Mo i $Sr_2Nb_2O_7$ har visat sig vara en mycket god kombination för att erhålla en fotokatalysator som är soljusaktiv med beräknade band gap på 2.14 och 2.94 eV för N och Mo nära och långt ifrån varandra. Vi kan också dra slutsatsen att den relativa stabiliteten där dopa-

tomerna är placerade nära varandra äs större än den när dopatomerna placeras långt ifrån varandra.

Metall-oxid ovh nitridytor såsom TiO_2, NiO and β-Si_3N_4 har undersökts för att dissociera en vattenmolekyl och för att adsorbera gasmolekyler (SO_2, NH_3, NO_2 and H_2S) till gassensorer. Vattenadsorption visar sig vara dissociativ på en syrefattig (001)- rutil nanotrådar på grund laddningsöverföringen från Ti-atomer på ytan till vattenmolekylen. Våra resultat ger en möjlig förklaring till den dissociation av vattenmolekyler som spontant sker på TiO_2 och (0001) β-Si_3N_4. Vidare visar våra beräkningar att defekter är involverade i adsorptionen av svaveldioxidmolekyler på (101)- och (001)- TiO_2-ytor, något som även bekräftats av Fourier Transform Infraröda (FTIR)-spektra. Fixering av svaveldioxidmolekyler på TiO_2-ytor har förklarat elektronstrukturen och ändingen av oxidationstillstånd via laddningsöverföring. NiO har föreslagits vara en god kandidat som gassensor för många farliga gaser såsom NO_2, H_2S och NH_3. Kemisorptionen av NO_2-molekyler på NiO-ytan är mycket stark jämfört med H_2S and NH_3 och ger upphov till nya tillstånd i bandgapet. H_2S-molekyler interagerar med (001)-NiO-ytan och bandgapet minskar något med ökande täckningsgrad, upp till 0.5 monolager. När det gäller adsorption av NH_3-molekyler ökar adsorptionsenergin med täckningsgraden och bandgapet är direkt relaterat till adsorptionsenergin. Analys av laddningsöverföringen mellangasmolekylerna och NiO-ytan har illustrerats med Bader-analys och med visualisering av laddningsfördelningen med hjälp av isoytor.

Den sista delen av min avhandling ägnas åt kaolinit och dess elektronstruktur. Många olika defekter har simulerats och de teoretiska resultaten har jämförts med experiment. Bandgapet för kaolinit och inverkan av olika defekter på elektronstrukturen har förutspåtts. Bandgapet för kaolinit beräknas ligga mellan 6.2 och 8.2 eV beroende på vilken beräkningsmetod som används.Vidare observeras att de defekter där syre ersätter väte i någon av hydroxylgrupperna i Al-terminerade (001)-ytorna (O_H) har lägre energi än de andra studerade defekterna när omgivningen är syrerik. Detta är en indikation på att O_H-defekten har lägre bildningsentalpi jämfört med övriga defekter. G_0W_0-metoden ger en god uppskattning av kaolinitens elektronstruktur, inklusive defekter och effekten av det "corehål" som bildas vid absorptionsprocessen. Detta möjliggör en noggrann uppskattning av NEXAFS-spectra.

Acknowledgements

Bibliography

1.   Lewis, N.S., et al., Proceedings of the National Academy of Sciences of the United States of America. **103**(43): p. 15729-15735 2006.
2.   Lewis, N.S., Science. **315**(5813): p. 798-801 2007.
3.   Crabtree, G.W., et al., Physics Today. **39** 2004.
4.   Grant, P.M., Nature. **424**(6945): p. 129-130 2003.
5.   Gamage, J., et al., International Journal of Photoenergy, 2010.
6.   Fujishima, A., et al., Nature. **238**(5358): p. 37-+ 1972.
7.   Takata, T., et al., Chemistry of Materials. **9**(5): p. 1063-& 1997.
8.   Ikeda, S., et al., Chemistry of Materials. **10**(1): p. 72-77 1998.
9.   Kudo, A., et al., Journal of Physical Chemistry B. **104**(3): p. 571-575 2000.
10.   Yoshino, M., et al., Chemistry of Materials. **14**(8): p. 3369-3376 2002.
11.   Miseki, Y., et al., Chemistry Letters. **35**(9): p. 1052-1053 2006.
12.   Asahi, R., et al., Science. **293**(5528): p. 269-271 2001.
13.   Kudo, A., et al., Chemical Physics Letters. **331**(5-6): p. 373-377 2000.
14.   Kato, H., et al., Journal of Physical Chemistry B. **105**(19): p. 4285-4292 2001.
15.   Gueymard, C.A., et al., Solar Energy. **73**(6): p. 443-467 2002.
16.   Choi, W.Y., et al., Journal of Physical Chemistry. **98**(51): p. 13669-13679 1994.
17.   Luque, A., et al., Physical Review Letters. **78**(26): p. 5014-5017 1997.
18.   Zhu, W.G., et al., Physical Review Letters. **103**(22) 2009.
19.   Shen, G., et al., Journal of Materials Chemistry. **19**(7): p. 828-839 2009.
20.   Linsebigler, A.L., et al., Chemical Reviews. **95**(3): p. 735-758 1995.
21.   Schaub, R., et al., Physical Review Letters. **87**(26) 2001.
22.   Henrich, V.E., et al., Applied Surface Science. **72**(4): p. 277-284 1993.
23.   Badmus, B.S., et al., International Journal of Physical Sciences. **4**(10): p. 592-606 2009.
24.   Murray, H.H., Applied Clay Science. **5**: p. 379 1991.
25.   Lee, S.J., et al., Applied Clay Science. **1**: p. 145 1985.
26.   He, M.C., et al., Chinese Physics Letters. **26**(5) 2009.
27.   Hohenberg, P., et al., Physical Review B. **136**(3B): p. B864-& 1964.
28.   Kohn, W., et al., Physical Review. **140**(4A): p. 1133-& 1965.
29.   Martin, R.M., Electronic structure: Basic theory and practical methods Cambridge University press, 2004.
30.   Ceperley, D.M., et al., Physical Review Letters. **45**(7): p. 566-569 1980.
31.   Tran, F., et al., Physical Review Letters. **102**(22) 2009.
32.   Perdew, J.P., et al., Physical Review Letters. **77**(18): p. 3865-3868 1996.
33.   Perdew, J.P., et al., Physical Review Letters. **100**(13) 2008.
34.   Perdew, J.P., et al., Physical Review B. **45**(23): p. 13244-13249 1992.

35.   Vanderbilt, D., Physical Review B. **41**(11): p. 7892-7895 1990.
36.   Hamann, D.R., et al., Physical Review Letters. **43**(20): p. 1494-1497 1979.
37.   Andersen, O.K., Physical Review B. **12**(8): p. 3060-3083 1975.
38.   Blochl, P.E., Physical Review B. **50**(24): p. 17953-17979 1994.
39.   Kresse, G., et al., Physical Review B. **59**(3): p. 1758-1775 1999.
40.   Aulbur, W.G., et al., Solid State Physics: Advances in Research and Applications, Vol. 54. **54**: p. 1-218 2000.
41.   Liechtenstein, A.I., et al., Physical Review B. **52**(8): p. R5467-R5470 1995.
42.   Shick, A.B., et al., Physical Review B. **60**(15): p. 10763-10769 1999.
43.   Marsman, M., et al., Journal of Physics-Condensed Matter. **20**(6) 2008.
44.   Perdew, J.P., et al., Journal of Chemical Physics. **105**(22): p. 9982-9985 1996.
45.   Becke, A.D., Journal of Chemical Physics. **98**(2): p. 1372-1377 1993.
46.   Bruneval, F., Physical Review Letters. **103**(17) 2009.
47.   Landau, L.D., Soviet Physics Jetp-Ussr. **8**(1): p. 70-74 1959.
48.   Hybertsen, M.S., et al., Physical Review Letters. **55**(13): p. 1418-1421 1985.
49.   Kajita, S., et al., Journal of Physics: Conference Series. **29**: p. 120 2006.
50.   Ramprasad, R., et al., Physical Review B. **60**(8): p. 6023-6027 1999.
51.   Weast, R.C., et al., Handbook of Physics and Chemistry 64th edn, D158 (CRC Press), 1983.
52.   Johansson, B., et al., Physical Review B. **21**(10): p. 4427-4457 1980.
53.   Brena, B., et al., Journal of Chemical Physics. **122**(18) 2005.
54.   Li, Q., et al., Physica B-Condensed Matter. **404**(12-13): p. 1643-1647 2009.
55.   Arhammar, C., et al., Proceedings of the National Academy of Sciences of the United States of America. **108**(16): p. 6355-6360 2011.
56.   Ambrosch-Draxl, C., et al., Computer Physics Communications. **175**(1): p. 1-14 2006.
57.   Gajdos, M., et al., Physical Review B. **73**(4) 2006.
58.   Persson, C., et al., Physical Review B. **72**(3) 2005.
59.   Zheng, J.X., et al., Physical Review B. **75**(10) 2007.
60.   Weast, R.C., et al., Handbook of Physics and Chemistry, 64th edn. **D158** (CRC Press, 1983).
61.   Zhang, R.Q., et al., Journal of Physical Chemistry C. **115**(8): p. 3425-3428 2011.
62.   Xu, Y., et al., American Mineralogist. **85**(3-4): p. 543-556 2000.
63.   Kudo, A., et al., Chemical Society Reviews. **38**(1): p. 253-278 2009.
64.   Chen, D., et al., Chemistry of Materials. **21**(11): p. 2327-2333 2009.
65.   Lin, W.H., et al., Applied Physics Letters. **89**(21) 2006.
66.   Dunkle, S.S., et al., Journal of Physical Chemistry C. **113**(24): p. 10341-10345 2009.
67.   Zou, Z.G., et al., Chemical Physics Letters. **343**(3-4): p. 303-308 2001.
68.   Shi, R., et al., Journal of Physical Chemistry C. **114**(14): p. 6472-6477 2010.
69.   Gai, Y.Q., et al., Physical Review Letters. **102**(3) 2009.
70.   Zou, Z.G., et al., International Journal of Hydrogen Energy. **28**(6): p. 663-669 2003.

71.   Zhou, X., et al., Journal of Physical Chemistry C. **115**(16): p. 8305-8311 2011.

72.   Wang, D.F., et al., Journal of the American Chemical Society. **130**(9): p. 2724-+ 2008.

73.   Maeda, K., et al., Nature. **440**(7082): p. 295-295 2006.

74.   Zou, Z.G., et al., Nature. **414**(6864): p. 625-627 2001.

75.   Wei, S.H., et al., Physical Review B. **32**(12): p. 7792-7797 1985.

76.   Godby, R.W., et al., Physical Review Letters. **56**(22): p. 2415-2418 1986.

77.   Yin, W.J., et al., Physical Review Letters. **106**(6) 2011.

78.   Long, R., et al., Chemphyschem. **12**(14): p. 2604-2608 2011.

79.   Qiu, X.Q., et al., Journal of the American Chemical Society. **132**(43): p. 15259-15267 2010.

80.   Yu, H.G., et al., Journal of the American Chemical Society. **132**(20): p. 6898-+ 2010.

81.   Kato, H., et al., Journal of the American Chemical Society. **125**(10): p. 3082-3089 2003.

82.   L.M. Torres-Martínez, R.G., O. Vázquez-Cuchillo, I. Juárez-Ramírez, A. Cruz-López, F.J. Alejandre-Sandoval, Catalysis Communications. **12**: p. 268 2010.

83.   Yi, Z.G., et al., Journal of Applied Physics. **106**(7) 2009.

84.   Iwase, A., et al., Bulletin of the Chemical Society of Japan. **82**(4): p. 514-518 2009.

85.   Long, R., et al., Chemical Physics Letters. **478**(4-6): p. 175-179 2009.

86.   Batzill, M., et al., Physical Chemistry Chemical Physics. **9**(19): p. 2307-2318 2007.

87.   Mulakaluri, N., et al., Physical Review Letters. **103**(17) 2009.

88.   Brookes, I.M., et al., Physical Review Letters. **87**(26) 2001.

89.   Wright, J.S., et al., Semiconductor Science and Technology. **25**(2) 2010.

90.   Yuan, Q.Z., et al., Journal of Physical Chemistry C. **113**(15): p. 6107-6113 2009.

91.   Chen, Y.J., et al., Applied Physics Letters. **87**(23) 2005.

92.   Wanbayor, R., et al., Materials Chemistry and Physics. **124**(1): p. 720-725 2010.

93.   Lüth, Solid Surfaces, Interfaces and Thin Films. Springer, Germany, 2001.

94.   Meyer, B., et al., Angewandte Chemie-International Edition. **43**(48): p. 6642-6645 2004.

95.   Hu, X.L., et al., Physical Chemistry Chemical Physics. **13**(48): p. 21652-21652 2011.

96.   Almeida, A.L., et al., Journal of Chemical Physics. **109**(9): p. 3671-3685 1998.

97.   Oviedo, J., et al., Journal of Physical Chemistry C. **112**(46): p. 17737-17740 2008.

98.   Zhang, Z., et al., Journal of Physical Chemistry B. **110**(43): p. 21840-21845 2006.

99.   Henderson, M.A., Surface Science Reports. **46**(1-8): p. 5-308 2002.

100.   Fubini, B., et al., Journal of Materials Science. **24**(2): p. 549-556 1989.

101. Bader, R., Atoms in Molecules: A Quantum Theory, Oxford University Press, New York, 1990.
102. Weltoncook, M.R., et al., Journal of Physics C-Solid State Physics. **13**(20): p. 3993-4000 1980.
103. Netzer, F.P., et al., Journal of Physics C-Solid State Physics. **8**(15): p. 2401-2412 1975.
104. Hotovy, I., et al., Sensors and Actuators B-Chemical. **78**(1-3): p. 126-132 2001.
105. Grim, R.E., Clay Mineralogy. McGraw-Hill, New York, 596 pp, 1968.
106. Neder, R.B., et al., Clays and Clay Minerals. **47**(4): p. 487-494 1999.
107. Coyne, L.M., Origins of Life and Evolution of the Biosphere. **15**(3): p. 161-206 1985.
108. Kameda, J., et al., American Mineralogist. **90**(8-9): p. 1462-1465 2005.

Acta Universitatis Upsaliensis

Digital Comprehensive Summaries of Uppsala Dissertations
from the Faculty of Science and Technology 958

Editor: The Dean of the Faculty of Science and Technology

A doctoral dissertation from the Faculty of Science and
Technology, Uppsala University, is usually a summary of a
number of papers. A few copies of the complete dissertation
are kept at major Swedish research libraries, while the
summary alone is distributed internationally through
the series Digital Comprehensive Summaries of Uppsala
Dissertations from the Faculty of Science and Technology.